ANKARA YILDIRIM BEYAZIT UNIVERSITY

GRADUATE SCHOOL OF NATURAL AND APPLIED SCIENCES



SYNTHESIS OF MOLYBDENUM CARBIDE THIN FILMS FOR PRODUCTION OF HYDROGEN VIA ELECTROCHEMICAL WATER SPLITTING

M.Sc. Thesis by

Cesur ALTINKAYA

Department of Energy Systems Engineering

July, 2018

ANKARA

SYNTHESIS OF MOLYBDENUM CARBIDE THIN FILMS FOR PRODUCTION OF HYDROGEN VIA ELECTROCHEMICAL WATER SPLITTING

A Thesis Submitted to

The Graduate School of Natural and Applied Sciences of

Ankara Yıldırım Beyazıt University

In Partial Fulfillment of the Requirements for the Degree of Master of Science in Energy Systems Engineering

by

Cesur ALTINKAYA

July, 2018

ANKARA

M.SC. THESIS EXAMINATION RESULT FORM

We have read the thesis entitled **"SYNTHESIS OF MOLYBDENUM CARBIDE THIN FILMS FOR PRODUCTION OF HYDROGEN VIA ELECTROCHEMICAL WATER SPLITTING"** completed by **CESUR ALTINKAYA** under the supervisions of **PROF. DR. ABDULLAH YILDIZ** and **ASSIST. PROF. DR. SAIM EMIN**, and we certify that in our opinion it is fully adequate, in scope and in quality, as a thesis for the degree of Master of Science.

Prof. Dr. Abdullah YILDIZ

Supervisor

Assist. Prof. Dr. Saim EMIN

Co-supervisor

Prof. Dr. Hasan OKUYUCU

Jury Member

Prof. Dr. Sefer Bora LİŞESİVDİN

Jury Member

Assist. Prof. Dr. Kouroush SALİMİ

Jury Member

Prof. Dr. Fatih V. ÇELEBİ

Director

Graduate School of Natural and Applied Sciences

ETHICAL DECLARATION

I hereby declare that, in this thesis which has been prepared in accordance with the Thesis Writing Manual of Graduate School of Natural and Applied Sciences,

- All data, information and documents are obtained in the framework of academic and ethical rules,
- All information, documents and assessments are presented in accordance with scientific ethics and morals,
- All the materials that have been utilized are fully cited and referenced,
- No change has been made on the utilized materials,
- All the works presented are original,

and in any contrary case of above statements, I accept to renounce all my legal rights.

July, 2018 **Cesur ALTINKAYA**

ACKNOWLEDGMENTS

Firstly, I would like to present my sincere gratitude to my supervisor, Prof. Dr. Abdullah YILDIZ, and my co-supervisor Assistant. Prof. Dr. Saim EMIN for their tremendous support and motivation during my study. Their deep knowledge and precious advice pave the way for this study. Their guidance assisted me all the time of my research including writing this thesis.

Also, I would like to thank the University of Nova Gorica and specifically the Material Research Laboratory. The doors of the lab were always open to me and all the researchers of the lab gave me all kinds of support during my thesis work. They were always very tactful and hospitable to me. I would like to the thank head of the laboratory, Prof. Dr. Matjaz Valant, and also Assist. Prof. Dr. Mattia Fanetti, Assist. Prof. Dr. Artem Badasyan, Mrs. Mojca Vrcon Mihelj, Mr. Andraz Mavric and Ms. Katja Ferfolja, individually.

Moreover, I would like to thank the members of my thesis committee, Prof. Dr. Hasan OKUYUCU, Prof. Dr. Sefer Bora LİŞESİVDİN, and Assist. Prof. Dr. Kouroush SALİMİ for their inspiration and profound comments. Also, I am grateful to my tutor, Mr. Thomas M. RYAN, for his very precious advice and patient towards me.

I am also thankful to my colleague Ali SEMERCİ who we worked together in the Material Research Laboratory. In addition, I would like to thank Abdullah ATILGAN and Aycan ATLI who are valuable researchers of Yıldız Research Group.

Finally, I would like to thank my mother, Kamile ALTINKAYA. I always feel her support and compassion in my heart. Also, I am thankful to my second mother, Gülden and my old sisters, Meryem, Resmiye, Cemile, Hanife, Ulviye, Gülkız, Nariye, Gulhan, Sultan, Emine, Duygu. They are almost like a source of power for me. As the last sentence, I would like to thank Ms. M. ÖNER for her excellent friendship and always supporting me.

Thank you.

2018, July **Cesur ALTINKAYA**

SYNTHESIS OF MOLYBDENUM CARBIDE THIN FILMS FOR PRODUCTION OF HYDROGEN VIA ELECTROCHEMICAL WATER SPLITTING

ABSTRACT

In this study, wet-chemical techniques were used to synthesize colloidal molybdenum nanoparticles (NPs). The synthesis of colloidal Molybdenum NPs was done by using pyrolysis of hexacarbonyl Molybdenum in 1-Octadecene under Argon atmosphere at 220 °C. Further, metallic Molybdenum and Molybdenum carbide catalysts were fabricated by spin coating of synthesized Molybdenum NPs onto graphite substrates and subsequent heat treatments at elevated temperatures under Argon atmosphere. For the first time, we achieved the fabrication of Molybdenum carbide thin films on graphite substrate from colloidal Molybdenum NPs without utilizing any reducing gas.

In addition, Platinum NPs were synthesized by pyrolysis of Platinum-bis(acetylacetonate) precursor and following subsequent heat treatments on graphite substrates. Prepared Platinum-based electrodes were used as a reference material towards hydrogen evolution reaction.

Characterization of Molybdenum, Platinum and Molybdenum carbide catalysts were carried out by using X-Ray Diffractometer, Transmission Electron Microscope, and Scanning Electron Microscope. Linear sweep voltammetry, cyclic voltammetry, chronoamperometry/chronopotentiometry and electrochemical impedance spectroscopy measurements were performed in a three-electrode cell in 0,5 molar sulfuric acid aqueous electrolyte solution (pH = 0). Molybdenum carbide thin films exhibit excellent catalytic activity and chemical stability for hydrogen evolution reactions.

Keywords: Molybdenum, platinum, molybdenum carbide thin films, hydrogen evolution reaction, HER, water splitting, electrolysis, electrochemistry, pyrolysis, thin films.

SUYUN ELEKTROKİMYASAL PARÇALANMASI YÖNTEMİYLE HİDROJEN ELDESİ İÇİN MOLİBDEN KARBİD İNCE FİLMLERİN SENTEZLENMESİ

ÖZET

Bu çalışmada kolloidal Molibden nanopartikülleri (NP'ler) ıslak kimyasal teknikler kullanılarak sentezlenmiştir. NP'lerin sentezi, Hekzakarbonilmolibdenin 1-Oktadesen içerisinde 220 °C'de Argon atmosferi altında pirolize edilmesiyle gerçekleştirilmiştir. Elde edilen Molibden NP'ler döndürmeli kaplama cihazı ile grafit alttaş üzerine kaplanarak yüksek sıcaklıklarda Argon atmosferi altında tüp fırın içinde tavlanmış ve böylece metalik Molibden ve Molibden karbür ince film elektrotlar üretilmiştir.

Platinum nanopartiküllerin sentezi, Molibden NP'lerin senteziyle aynı teknikler kullanılarak platin-bis asetilasetonat öncüsünün piroliziyle elde edildi ve grafit alttaşlar üzerine kaplanarak yüksek sıcaklıklarda ısıl işleme tabi tutuldu. Elde edilen Platin ince film elektrotlar, Molibden karbidin hidrojen eldesindeki katalitik aktivitesini göstermek için referans olarak kullanıldı.

Üretilen Molibden ve Platin NP'ler ile molinden karbid ince filmlerin yapısal ve morfolojik özellikleri X-Işını Kırınımı, Taramalı Elektron Mikroskobu ve Transmisyon Elektron Mikroskobu kullanılarak incelendi. Lineer tarama voltametrisi, dögüsel voltametri, empedans spektroskopisi ve dayanıklıklık testleri ise üç-elektrot konfigürasyonu kullanılarak 0.5 molar sülfürik asit elektrolit çözeltisi içerisinde gerçekleşleştirildi. Sonuç olarak, Molibden karbid ince film elektrotların elektroliz yöntemiyle hidrojen üretiminde kullanılmak için mükemmel katalitik aktivite ve kimyasal dayanaklılığa sahip oldukları ortaya çıktı.

Anahtar Kelimeler: Molibden, patin, molibden karbid ince film, hidrojen eldesi reaksiyonu, suyun parçalanması, elektroliz, elektrokimya, piroliz, ince filmler.

CONTENTS

M.SC. THESIS EXAMINATION RESULT FORM ii
ETHICAL DECLARATİON iii
ACKNOWLEDGMENTS iv
ABSTRACT v
NOMENCLATURE ix
LIST OF TABLES xi
LIST OF FIGURES xii
CHAPTER 1 - INTRODUCTION 1
CHAPTER 2 - WATER ELECTROLYSIS 3
2.1 Working Principle 3
2.2 Thermodynamic Aspects 4
2.3 Catalyst and Electrolyte Properties 8
2.4 Choosing an Electrocatalyst 10
2.5 Overpotential 11
2.6 Mechanisms: Volmer, Tafel and Heyrovsky 13
CHAPTER 3- EXPERIMENTAL STUDIES 15
3.1 Materials 15
3.2 Synthesis of Mo Nanoparticles (NPs) 15
3.3 Synthesis of Pt NPs 16
3.4 Cleaning of Graphite Substrates 17
3.5 Deposition of Mo and Pt NPs 18
3.6 Annealing of Textured Mo and Pt Catalysts 18
3.7 Attaching Electric Wires 20
CHAPTER 4 - CHARACTERIZATION METHODS 21
4.1 X-Ray Diffraction (XRD) Measurements 21
4.2 Transmission Electron Microscopy (TEM) 21
4.3 Scanning Electron Microscopy (SEM) 22
4.4 Electrochemical Measurements 23
4.5 Impedance Spectroscopy 24
4.6 Stability Tests 24
CHAPTER 5 - RESULTS AND DISCUSSIONS 26
5.1 XRD Pattern of Bare Graphite 26

5.2 XRD Pattern of Pt-based Electrodes 26
5.3 XRD Pattern of Mo NPs 27
5.4 XRD Pattern of Mo-based Electrodes 28
5.5 TEM Images of Pt NPs 30
5.6 TEM Images and EDS Maps of Mo NPs 31
5.7 SEM Images of Bare Graphite Substrate 32
5.8 SEM Images of Pt-based Samples 33
5.9 SEM Images and EDS Maps of Mo-G800 Sample 34
5.10 SEM Images of Mo-based Samples 36
5.11 CV Curve of Mo-G800 Sample 38
5.12 CV Curve of Mo-G900 Sample 39
5.13 LSV Curve of Pt-based Electrodes and Bare Graphite Substrate 40
5.14 LSV Curves of Mo-based Electrodes 41
5.15 Tafel Slopes of Prepared Electrodes 43
5.16 Stability Tests of Mo-G800 and Mo-G900 Samples 45
5.17 Electrochemical Impedance Spectroscopy of Mo-G800 Sample 46
CHAPTER 6 - CONCLUSİON 48
REFERENCES 49
CURRICULUM VITAE 56

NOMENCLATURE

Roman Letter Symbols

j	Current density
j_o	Exchange current density
I	Current
V	Potential
E_c	Cathodic cell potential
E_a	Anodic cell potential
E_{cell}	Cell potential
E_{act}	Activation potential
E_{rev}	Reversible potential
E_{tn}	Thermoneutral voltage
η	Overpotential
b	Tafel slope
Δ	Small change
Q	Total electric charge
S	Entropy
H	Enthalpy
G	Gibbs free energy
R	Universal gas constant/total ohmic resistance
T	Temperature
K	Kelvin
F	Faraday constant
C	Coulomb
μ	Chemical potential
p	Partial pressure
α	Chemical activity of water
R_{ct}	Charge transfer resistance
λ	X-ray wavelength
θ	Diffraction angle
M	Electrode surface
H_{ads}	Adsorbed hydrogen on electrode surface
k	Rate constant

R_{ct}	Charge transfer resistance
C_d	Double layer capacitance
Subscripts	
l	Liquid
g	Gas
aq	Aqueous
Acronyms	
HER	Hydrogen evolution reaction
OER	Oxygen evolution reaction
RHE	Reversible hydrogen electrode
NPs	Nanoparticles
XRD	X-ray Diffraction
SEM	Scanning electron microscopy
TEM	Transmission electron microscopy
HRTEM	High resolution transmission electron microscopy
LSV	Linear sweep voltammetry
CV	Cyclic voltammetry
EIS	Electrochemical impedance spectroscopy

LIST OF TABLES

Table 2.1 Important properties of a good electrocatalyst 10
Table 2.2 Important properties of a good electrolyte solution 10
Table 3.1 Annealing details and nomenclature of Mo- and Pt-based electrodes 19
Table 5.1 Catalytic activity results of prepared electrodes..... 44
Table 5.2 Electrochemical impedance spectroscopy results of Mo-G800 sample 47

LIST OF FIGURES

Figure 2.1 Simple water electrolysis cell 4
Figure 2.2 Temperature dependent cell potential for hydrogen generation 7
Figure 2.3 Change of reversible cell potential at elevated temperature and pressure . 7
Figure 2.4 Difference in the catalyzed and uncatalyzed reaction pathways 8
Figure 2.5 The process of common electrochemical reaction..... 9
Figure 2.6 Metal-hydrogen bond strength of different metals 11
Figure 2.7 Energy diagram of electrolysis cell. 12
Figure 2.8 Steps involved in HER mechanism and relative Tafel slope..... 14
Figure 3.1 Synthesis setup of Mo and Pt NPs..... 16
Figure 3.2 Images taken during synthesis of NPs 17
Figure 3.3 Images of graphite substrates and sandpaper..... 17
Figure 3.4 Spin coating application scheme..... 18
Figure 3.5 Images of the utilized oven and obtained Mo-based electrodes 18
Figure 3.6 The annealing scheme of electrodes in the oven. 19
Figure 3.7 Schematic and real images of prepared electrodes 20
Figure 4.1 Rigaku Miniflex 600 Powder X-ray Diffractometer..... 21
Figure 4.2 JEOL-2100 F Transmission Electron Microscopy setup..... 22
Figure 4.3 JEOL JSM-7100 F Scanning Electron Microscopy setup 22
Figure 4.4 Three-electrode configuration and related electrodes..... 23
Figure 4.5 Three-electrode configuration with Nafion membrane 24
Figure 4.6 Image of prepared electrodes for stability test..... 25
Figure 4.7 O_2 and H_2 generation during stability test of Mo-G800 sample. 25
Figure 5.1 XRD pattern of bare graphite substrate and synthesized Pt NPs..... 26
Figure 5.2 XRD pattern of Pt-based electrodes..... 27
Figure 5.3 XRD pattern of as-synthesized Mo NPs. 28
Figure 5.4 Phase diagram of Mo-C 28
Figure 5.5 XRD pattern of Mo-based electrodes 29
Figure 5.6 TEM) and HRTEM images of Pt NPs 30
Figure 5.7 TEM images of Mo NPs 31
Figure 5.8 TEM image and corresponding elemental maps of Mo NPs. 32
Figure 5.9 SEM images of bare graphite substrate 33
Figure 5.10 SEM images of Pt-G500 sample..... 33

Figure 5.11 SEM images of Pt-G1000 sample 34
Figure 5.12 SEM images of Mo-G800 sample 35
Figure 5.13 SEM image and corresponding EDS mapping of Mo-G800 sample..... 35
Figure 5.14 SEM images of Mo-based samples..... 36
Figure 5.15 SEM images and corresponding particle sizes of Mo-based samples . 37
Figure 5.16 SEM image and elemental maps of Mo-based samples 38
Figure 5.17 CV curve of Mo-G800 sample 39
Figure 5.18 CV curves of Mo-G900 sample. 40
Figure 5.19 LSV curves of Pt-based samples 41
Figure 5.20 LSV curves Mo-based electrodes 42
Figure 5.21 LSV curves of Mo-based electrodes..... 43
Figure 5.22 Tafel slopes of Mo-based electrodes and Pt-G1000 sample..... 44
Figure 5.23 LSV curves of Mo-G800 sample before and after1000 CV cycles 45
Figure 5.24 LSV curves of Mo-G900 sample before and after 1000 CV cycles 46
Figure 5.25 Electrochemical impedance spectroscopy plots of Mo-G800 sample... 47

CHAPTER 1

INTRODUCTION

The increase in human population and constantly developing industrial technology are causing the world's energy demand to continually increase. Today, a large part of this energy demand is met by fossil fuels such as coal, natural gas and petroleum. But the fact that most of these fuels are located in certain countries, that their resources are limited, and the gradual depletion of their reserves, creates a huge energy problem. On the other hand, harmful gases such as SO_x, NO_x and CO_x which are produced as a result of using fossil fuels cause acid rain, forest destruction, ozone layer depletion and global warming due to the greenhouse effect. In conclusion, fossil fuels have negative effects on the environment and human health and threaten the future of our world. For all these reasons, the need for renewable energy sources that do not have a negative impact on the environment and human beings while meeting their growing energy need is increasing [1-4] .

Renewable energy sources such as solar, wind and hydropower are emerging as alternative energy sources to fossil fuels with the help of developing technology. However, the fact that these sources are not constant energy sources has become a huge problem because of their intermittent nature and fluctuations in production that change with years, seasons, months, days and regions [5]. Some of these problems include the fact that wind energy cannot be used for energy production at all locations in the world, and production where it is available can vary depending on the season; solar energy does not have enough efficiency in the polar regions of the world, and hydropower has very limited resources in areas close to the equator. Because of these drawbacks hydrogen emerges as an important energy carrier.

Hydrogen is not a primary energy source that exists in nature. It is produced from other sources like water or hydrocarbons, and it requires energy in order to produce it. It can be an important energy carrier when it is produced using a renewable energy source [6, 7]. Hydrogen’s most important advantages are that it has much higher heating values compared to other fuels and can be stored, unlike electricity [8, 9]. For example;

when solar energy is produced, the excess energy generated during times when the sunlight is very high can be stored in the chemical bonds of the hydrogen, and this stored energy can be turned into electrical energy when needed.

Although there are various hydrogen production methods such as steam reforming, partial oxidation, coal gasification, water thermolysis, and photolysis, the hydrogen generation by water splitting is one of the most effective methods and has attracted great interest, recently [10]. The reasons for the latter are very simple: (i) it is not based on fossil fuels, (ii) it does not require very high temperatures, (iii) it is carried out at the ambient temperature, (iv) there is no need for very complicated technology and (v) purity of generated hydrogen is high. Briefly, the water splitting occurs as follows: The potential supplied from an external source is used to divided water into its components, hydrogen accumulated at the cathode while oxygen collected at the anode [11-13].

There is a need for a good cathode material for efficient hydrogen evolution reaction (HER). Platinum (Pt) group metals are known as the most efficient HER catalysts, but their occurrence in low amount in earth's crust and their high prices have led to the need for finding electrocatalysts which are cheap and available in sufficient quantities. Due to the fact that some transition elements have closed d-bands, their carbide phases have emerged as the most important candidates to replace Pt in terms of cost. [14-16]. In this context, catalysts produced especially from molybdenum carbides have attracted great interest in recent years. The reason for this is that they have both high catalytic activity and high durability in both acidic and basic conditions for HER [17-19].

In this thesis, molybdenum carbide (Mo_2C) catalysts have been tested for HER by means of water electrolysis. They were demonstrated high activity and stability towards HER. Although many studies on these transition metal carbides have been carried out in the literature, the synthesis methods of all of them are very tedious, long time consuming and use of CH_4 and H_2 as reducing agent [20]. In this thesis, we developed a novel procedure for the preparation of molybdenum carbide catalysts which demonstrated high catalytic activity for HER.

CHAPTER 2

2 WATER ELECTROLYSIS

2.1 Working Principle

Passing a direct current through two electrodes submerged in an electrolyte forms the basis of water splitting. During this process, hydrogen is accumulated at the cathode (negative pole) while oxygen is collected at the anode (positive pole). The current flowing through the electrodes determines the amount of hydrogen generation. Basically, Faraday's laws declare that:

1. The mass of material changed at an electrode at the time of electrolysis is proportional to the amount of electric charge (Q) transferred.

2. The amount of elemental material that is changed during electrolysis at an electrode has a direct proportion to the equivalent weight of the element for a given Q load. The equivalent weight of the material is obtained by dividing the molar mass by the oxidation state change in the case of electrolysis [21]

Water electrolysis has a great potential for energy production and use. A water electrolyser consists of two electrodes that produce hydrogen and oxygen as a result of electrochemical reactions, and an electrolyte that eases the transfer of ionic species from one electrode to another. The most important benefit of water electrolysis is that product gases can be easily accumulated separately by inserting an ion-conducting, gas-impermeable membrane between the electrodes where oxidation (oxygen evolution reaction, OER) and reduction (hydrogen evolution reaction, HER) happen [22].

The equation for oxygen and hydrogen gas production by passing electric current through water molecules is given below and this equation is the basic equation for electrolysis of water:

$$H_2O_{(l)} + \underbrace{237.2kjmol^{-1}}_{electricity} + \underbrace{48.6kjmol^{-1}}_{heat} \rightarrow H_2 + \frac{1}{2}O_2 \quad [23] \qquad \textbf{(2.1)}$$

Figure 2.1 shows a scheme of an electrolyser with the two electrodes, called anodes and cathodes, electrolyte liquid and an external power supply connection [24]. An electrolyser has to meet some requisites for instance high efficiency, low cost and wide operational range [25].

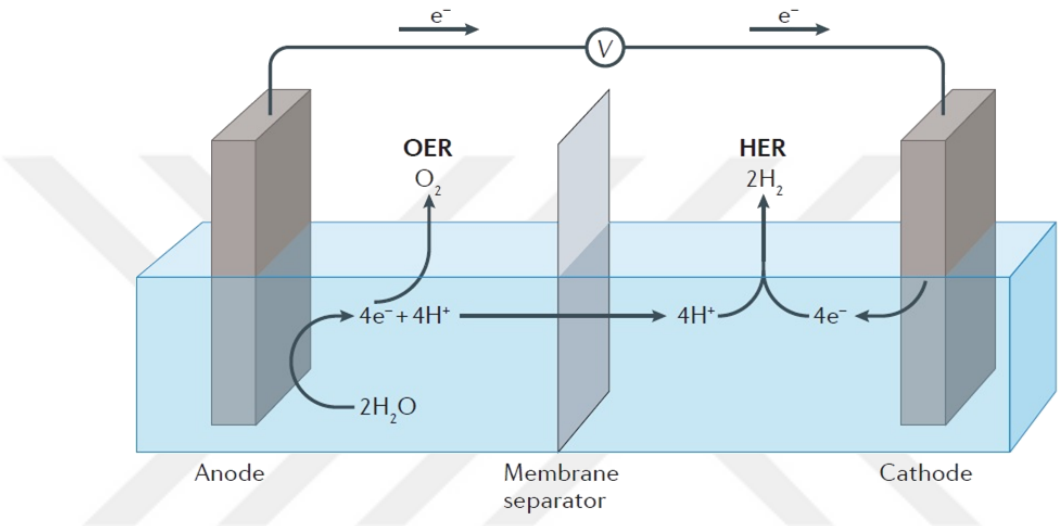


Figure 2.1 Simple water electrolysis cell [26]. Note: Membrane separator is optional

2.2 Thermodynamic Aspects

An electrochemical cell operates in regard to a reductive half reaction on the cathode and an oxidative half-reaction on the anode as seen in the following equations [27].

Anode $$2H_2O_l \rightarrow O_{2(g)} + 4H^+_{aq} + 4e^- \quad E^\circ_a = 1.23V \qquad \textbf{(2.2)}$$

Cathode $$2H^+_{aq} + 2e^- \rightarrow H_{2g} \quad E^\circ_c = 0V \qquad \textbf{(2.3)}$$

In this thesis, (°) always will introduce standard state conditions which are for the temperature at 25 °C (298 K), for liquid concentrations at 1M and for gas pressure at 1 atm.

According to equation 2.2-3, the standard cell potential, $E°$ ($E°_{cell}$), is determined by subtracting the standard anodic cell potential, $E°_a$, from the standard cathodic cell potential, $E°_c$.

$$\Delta E° = E°_{cell} = E° = E°_c - E°_a = -1.23V \quad \textbf{(2.4)}$$

Electrolysis is a chemical reaction of endothermic ($\Delta H > 0$) and non-spontaneous ($\Delta G > 0$) nature. During operation within the cell, H_2O starts to decompose when a certain voltage or "critical voltage" is applied across the electrodes. The amount of hydrogen generated per unit of water is directly proportional to the current applied in the system. The energy required for the reaction under standard temperature and pressure is determined by enthalpy change (ΔH). The next equation demonstrates the thermodynamic relationship inside the electrolysis cell.

$$\Delta G = \Delta H - Q = \Delta H - T \times \Delta S \quad \textbf{(2.5)}$$

In the above equation, ΔG is the Gibbs free energy change in the electric form of electricity. Q is the required thermal energy, which is equal to the yield of the reaction temperature, T and entropy change, ΔS.

A balanced chemical system is expressed as follows;

$$\Delta G = 0 \quad \textbf{(2.6)}$$

A real world chemical system cannot operate in this conditions. The Equilibrium condition for an electrochemical system is explained by

$$\Delta G = -nF\Delta E \quad \textbf{(2.7)}$$

where n is the number of moles of electrons participating in the conversion of 1 mole of product, F is the Faraday constant ($96485\ Cmol^{-1}$) and ΔE is the potential difference measured between the anode and cathode out of the standard conditions. If we examine the Eq. 2.7, reaction which runs to the right in the electrolyser, the minimum potential difference between water electrodes without resulting electrolysis;

$$\Delta E = \frac{\Delta G}{nF} \quad \textbf{(2.8)}$$

where n (for hydrogen, $n = 2$) is the number of moles of electrons transferred in the reaction.

$$\Delta G = \mu_{H_2} + \frac{1}{2}\mu_{O_2} - \mu_{H_2O} \quad \textbf{(2.9)}$$

İn the above equation, μ is the chemical potential of ingredients involved in equation for hydrogen, oxygen and water. From eq. 2.8 and 2.9, it can be derived [28];

$$\Delta E = \frac{\Delta G°}{2F} + \frac{RT}{2F}\ln\left(\frac{p_{h_2} \times p_{o_2}^{\frac{1}{2}}}{a_{H_2O}}\right) \quad \textbf{(2.10)}$$

where p is the partial pressure of the ingredients, R is the universal gas constant ($8.314\ J\ mol^{-1}K^{-1}$) and a_{H_2O} is the activity of water. Under standard conditions; $\Delta G = \Delta G° = 237.178\ kJ\ mol^{-1}$:

$$\Delta E° = \frac{237.178}{2 \times 96.485} = 1.229V \quad \textbf{(2.11)}$$

The water splitting is an endothermic reaction in which the total quantity of energy required in water electrolysis equals the alteration in enthalpy ($\Delta H = 286\ kJ / mol$). To obtain $\Delta H°$, the remaining energy needed can be provided by heat ($T\Delta S° = \Delta H°$). For this reason, the total energy requirement can be explained by the thermo-neutral cell voltage equation below;

$$\Delta E_{tn} = \frac{\Delta H°}{n \times F} = \frac{286000J}{2 \times 96485C} = 1.482V \quad \textbf{(2.12)}$$

For both $\Delta E°$and $\Delta E_{tn}°$, the total energy requirement varies slightly with temperature. For instance; $\Delta E°$ and $\Delta E_{tn}°$ is $1.229V$ and $1.482V$ under standard conditions, respectively. On the other hand, $\Delta E°$ and $\Delta E_{tn}°$ decrease to $1.184V$ and $1.473V$ at 80° C, respectively [29].

No net heat exchange occurs with the surroundings, when the cell potential, E_{cell} is equivalent to the thermoneutral voltage. If $E_{cell} < E_{tn}$, the cell receives heat from the surroundings, while cooling of the cell is necessary when $E_{cell} > E_{tn}$ [30].

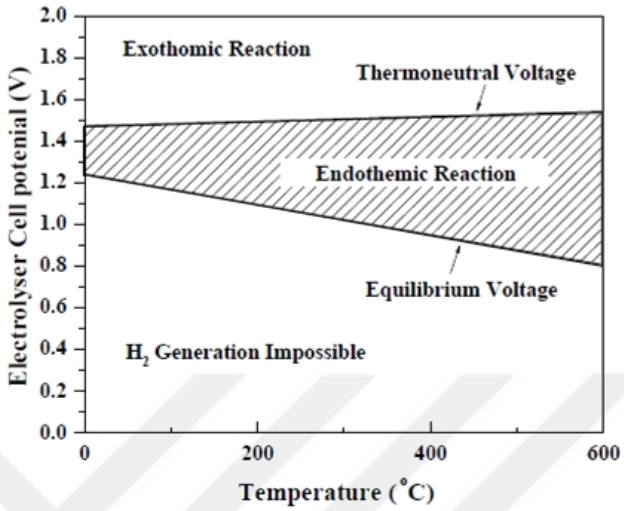


Figure 2.2 Temperature dependent cell potential for an ideal electrocatalytic hydrogen generation [31]

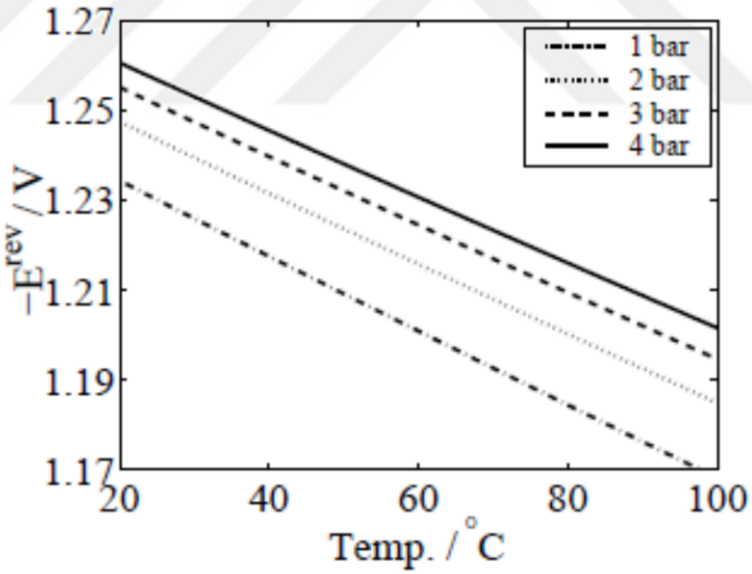


Figure 2.3 Change of reversible cell potential (ph=0) at elevated temperature and pressure [32]

Fig. 2.2 shows that the ideal voltage required to break water molecules decreases with increasing cell temperature. Hydrogen production is not possible if the cell voltage is below the reversible voltage. The real lowest voltage that must be supplied to the electrolytic cell is the thermoneutral voltage, and below this voltage the reaction is endothermic, while above this voltage it is exothermic and results in excess heat. If

electrolysis occurs in the shaded section in the figure, the efficiency will be 100% and the water separation will occur by soaking up heat from the surroundings [33]. On the other hand, it can be clearly seen that in Fig 2.3, when the pressure increases, reversible cell potential decreases.

2.3 Catalyst and Electrolyte Properties

A conventional catalyst lowers the Gibbs activation energy by providing a new pathway and, thus, accelerates the reaction. In the meantime, a reaction that is thermodynamically impossible cannot be made possible with the help of a catalyst. The intermediates formed during the reaction must be less stable than the products, otherwise the reaction will stop (dotted line in Figure 2.4) and the intermediates become the final products.

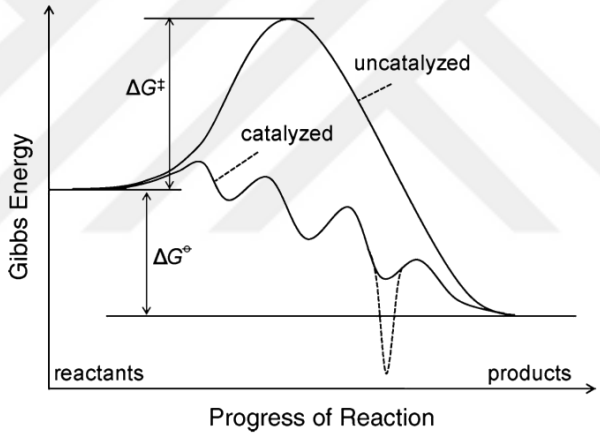


Figure 2.4 Difference in the catalyzed and uncatalyzed reaction pathways [34]

The electrochemical reaction process is demonstrated in Fig. 2.5. First, the mass transport which is movement of the reactant from the bulk solution to the electrode surface region (electrode interface) occurs. Then, when a potential different from the potential at steady condition is supplied to the cell, this potential difference results in electron exchange between the electrode and species in the electrolyte, thus electrolysis takes place.

$$i = nAFj \tag{2.13}$$

In equation 2.8, i is the current resulting from the electrolysis, n is the number of electrons per molecule participating in the reaction, A is the electrode surface area, F

is the Faraday constant and j is flux of species in solution. The flux, j, efficaciously mirrors the amount of material reaching the surface of the electrode per second as described below;

$$j = k(n)[Reactant]_0 \quad \textbf{(2.14)}$$

where $k(n)$ is the $n\text{-}th$ order rate constant for the electron transfer reaction and $[Reactant]_0$ is the concentration of the electro-active reactant species at the electrode surface (and not in the bulk solution) [35].

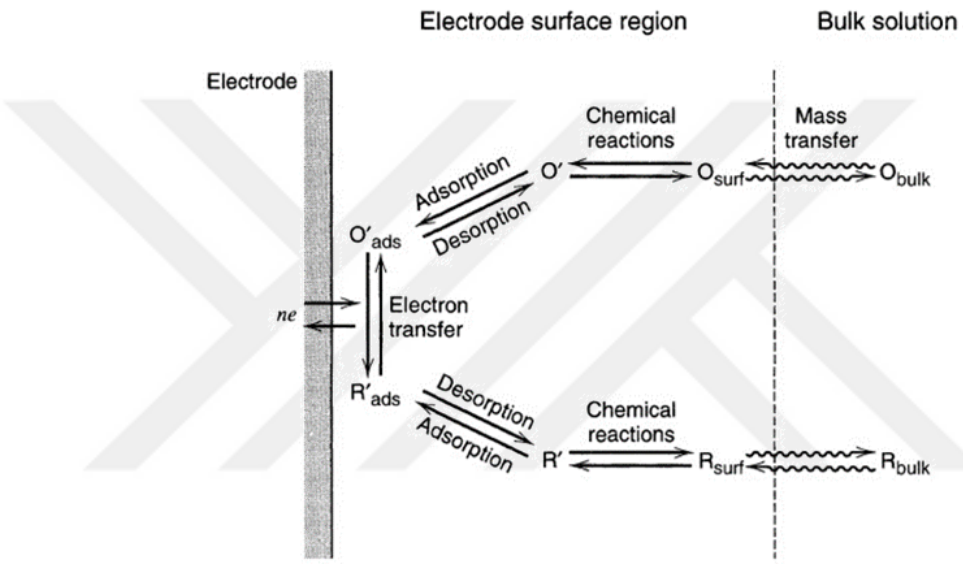


Figure 2.5 The process of common electrochemical reaction.[36]. Note: O refers to oxidized species and R refers to reduced species

An electrocatalyst is like a conventional catalyst; it accelerates a reaction without using itself up during the reaction and lowers the activation energy. Electrocatalysts are used in reactions where a net charge transfer occurs, therefore electron conductivity is an important parameter for electrocatalysts. Some important properties that must be provided to achieve good electrocatalyst and electrolyte compatibility as shown in Table 2.1 and 2.2 [37].

Table 2.1 Important properties of a good electrocatalyst

Property	Incentive
High surface area of catalyst	To increase the performance
Good electrocatalytic properties	To enhanced kinetics enhances performances
High electronic conductivity	In order to transport electrons to /from the electrode reaction
Sufficient porosity and pore size	To facilitate transportation of reactant and products
Long-term mechanical and chemical staability	Stability of both catalyst and electrode at elevated temperatures and potentials

Table 2.2 Important properties of a good electrolyte solution

Property	Incentive
Chemically stable	During electrolysis the electrolyte has to withstand harsh conditions like elevated temperatures, elevated potentials, extreme pHs and reactive species (O_2, H_2, etc.)
Ionic conductivity	High ionic conductivity to reduce ohmic resistances
Price	In order to commercialize the cost of the electrolyte need to be minimized

2.4 Choosing an Electrocatalyst

Adsorption is the basic chemical process in electrolysis which connects the reactants to the active sites of the catalyst. Adsorption is divided into two types; physisorption and chemisorption. The first type, physisorption, is dependent on weak Van der Waals bonds between the adsorbates and the catalyst active sites. In the second one, chemisorption, stronger chemical bonds are formed between the active sites of catalysts and adsorbates. Chemisorption is an important driving force in electrolysis. For an efficient process, the catalyst and the adsorbates should not be bonded to each other either weakly or very strongly because if they are weakly bonded, the process is not efficient and if they are strongly bonded, the entire surface may be coated with the

adsorbates, preventing access to active sites [38]. İn water-based hydrogen evolution reactions, hydrogen atoms should not be bonded either weakly or too strongly to the cathode surface. Fig. 2.8 shows catalytic activity of some metals for HER in terms of metal-hydrogen bond strength.

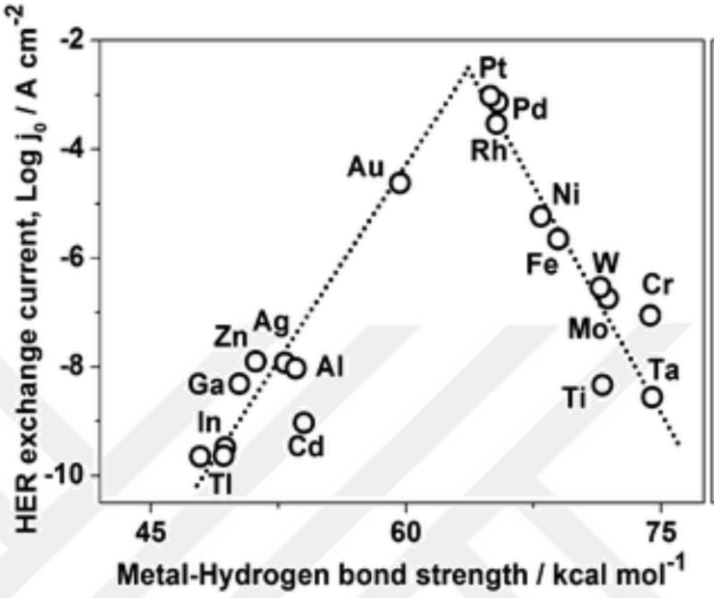


Figure 2.6 Metal-hydrogen bond strength of different metals [39]

2.5 Overpotential

The difference between real and theoretical potential is defined as an overpotential (see Fig. 2.9). In other words, overpotential can be defined as the voltage that has to be applied over the thermoneutral voltage (1.48 volts) to perform the electrolysis in real world conditions.

$$\Delta E = \Delta G + IR + \sum \eta \qquad \textbf{(2.15)}$$

In Eq. 2.15, ΔE and ΔG are cell voltage and Gibbs free energy for systems operating outside standard conditions, I is the driving current due to applied voltage, R is the sum of ohmic resistance resulting from electric cables, electrolyte and electrode resistance effects. $\sum \eta$ represents the total of overpotentials including the activation overpotentials at the anode and cathode, as well as concentration overpotential that originates from mass transport of the gaseous products away from the electrode surfaces [40].

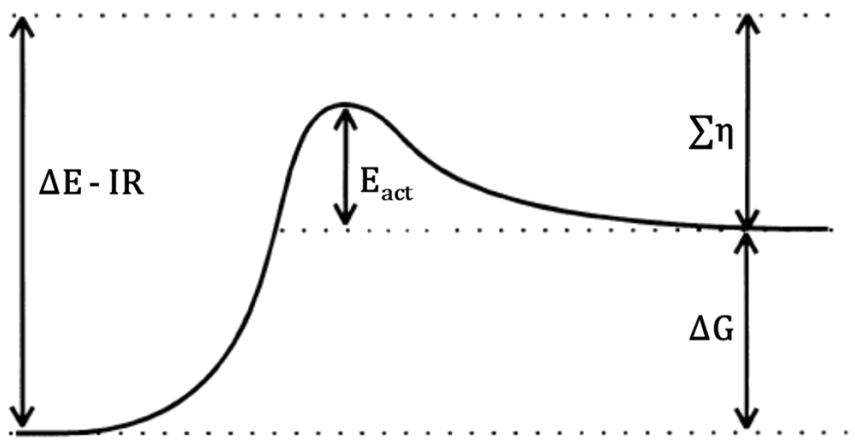


Figure 2.7 Energy diagram of electrolysis cell. (Adapted from [41])

In electrolysis, the cell delivers heat to the outside at voltages above 1.47 volts, while taking in the heats at voltages below 1.48 volts. For this reason, overvoltage should be kept at a low level to maximize efficiency and minimize heat generation. Hydrogen production at low overpotential levels will also be low, so the way to increase the efficiency without increasing the overpotential is to produce electrodes with high catalytic activity [41].

The overpotential is frequently given by the Tafel equation,

$$\eta = a + blog[\frac{j}{j_0}] \quad \textbf{(2.16)}$$

η is the overpotential, j is the current density, j_0 is exchange current density which is the current density at zero overpotential and b is the so-called Tafel slope.

$$b = \frac{\ln(10)\, RT}{a\eta F} \quad \textbf{(2.17)}$$

where R is the universal gas constant, T is the temperature, α is the so-called charge transfer coefficient, which must be between 0 and 1 and usually is assumed to be 0.5, n is the number of transferred electrons and F is Faraday's constant [42].

2.6 Mechanisms: Volmer, Tafel and Heyrovsky

The hydrogen evolution reaction is a fundamental reaction in electrochemistry. It takes place at the cathode of an electrolytic cell. The chemical reaction is rather simple: two protons are reduced to a dihydrogen molecule employing two electrons. The multi-step mechanism of the HER can be divided into the following steps. The reaction schemes show the HER in acidic solution which is similar to the processes in alkaline media

1. Transport of H^+ to the cathode surface
2. Electrochemical adsorption of H^+ on the electrode surface: Volmer reaction

$$M + H^+ + e \rightarrow H_{ads} \quad \textbf{(2.18)}$$

3. Formation and desorption of H_2 either a) electrochemically or b) chemically:
    a) Electrochemical desorption of H_2: Heyrovsky reaction

$$MH_{ads} + MH_{ads} \rightarrow M + H_2 \quad \textbf{(2.19)}$$

    b) Chemical desorption of H_2: Tafel reaction

$$MH_{ads} + MH_{ads} \rightarrow 2M + H_2 \quad \textbf{(2.20)}$$

4. Mass transport of H_2 away from the cathode

MH_{ads} denotes a H atom which is chemically adsorbed on an active site of an electrode M. The reaction pathway of the H_2 desorption strongly depends on intrinsic chemical and electronic properties of the catalyst. The rate-controlling step of the reaction at the electrode can be determined by the so-called Tafel-slope as shown in 2.10.

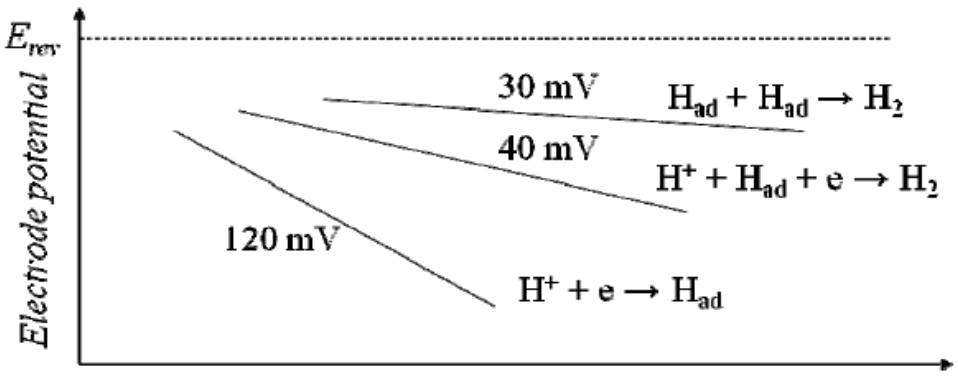


Figure 2.8 Steps involved in HER mechanism and relative Tafel slope [43]

The initial discharge step (2.18), involving an adsorbed H intermediate, H_{ads}, is followed by either the recombination of the H_{ads} (2.19) or electrochemical desorption of H_{ads} to form H_2 (2.20). Depending on the electrocatalytic properties of the electrode material, H_2 evolution proceeds through (2.18) +(2.19) or (2. 18)+(2. 20). Thus, the adsorbed intermediate can undergo either of two alternative pathways, depending on the nature of the electrode [43]

CHAPTER 3

3 EXPERIMENTAL STUDIES

3.1 Materials

Hexacarbonylmolybdenum (98%, $Mo(CO)_6$) Platinum(II) 2,4-pentanedionate ($Pt(C_5H_7O_2)_2$), oleic acid (99%, OA), oleylamine (70%, OLA), 1-octadecene (90%, ODE), chloroform (99.5%, $CHCl_3$), and ethanol (98%, EtOH) were procured from Alfa Aeser, UK. 2- Propanol (99.8%) was bought from VWR Chemicals, USA. Coiled Pt wire (99.999%) and Ag/AgCl electrode were bought from Sigma-Aldrich, Germany. Graphite block (99.9%) used for electrode preparation was procured from Beijing Great Wall Co, China. CloraCit Powder and ClaroCit Liquid were bought from Struers, Denmark.

3.2 Synthesis of Mo Nanoparticles (NPs)

Synthesis of Mo NPs was adapted from ref [44]. 1.056g (4.0 mmol) $Mo(CO)_6$, 0.22g OA (2 mmol) OA, 1.06g (4 mmol) OLA and 25 ml ODE was dissolved in a three-neck flask. Prior to dissolving, the empty flask was preheated to 120 °C to prevent aggregations that may occur at lower temeperatures. After waiting at this temperature until the $Mo(CO)_6$ is dissolved, the temperature was increased to 220 °C over 10 min and held at that temperature for 1h. The proof of formation for Mo NPs is the color change from light yellow to black. Once the reaction was completed the flask was left to cool to 80 °C. All heating and cooling procedures were made under Ar atmosphere and a magnetic stirrer was used during the reaction (see Fig. 3.1 for synthesis setup).

The cooled solution was filtered by using quantitative filter paper to separate from sediments. A mixture of EtOH:$CHCl_3$:2-Propanol (40:5:5 ml) was added to the filtered Mo NPs suspension. Then the suspension was centrifuged at 9000 rpm for 10 min. This process was repeated several times until clean and dark Mo NPs precipitate remained in the bottom of the centrifuge tube. Next, the precipitate was kept for 30

min at 40 °C in oven until it became black powder. After drying, 0.35 g of powdered Mo NPs were weighted (see Fig.3.2 for synthesis steps of Mo NPs).

Obtained NPs were redissolved in 3 ml $CHCl_3$ to ensure homogenous dispersion of NPs and, thus to achieve proper thin film coatings on graphite substrate. Finally, the Mo NPs suspension was filtered using 0.45 μm PTFE syringe filter.

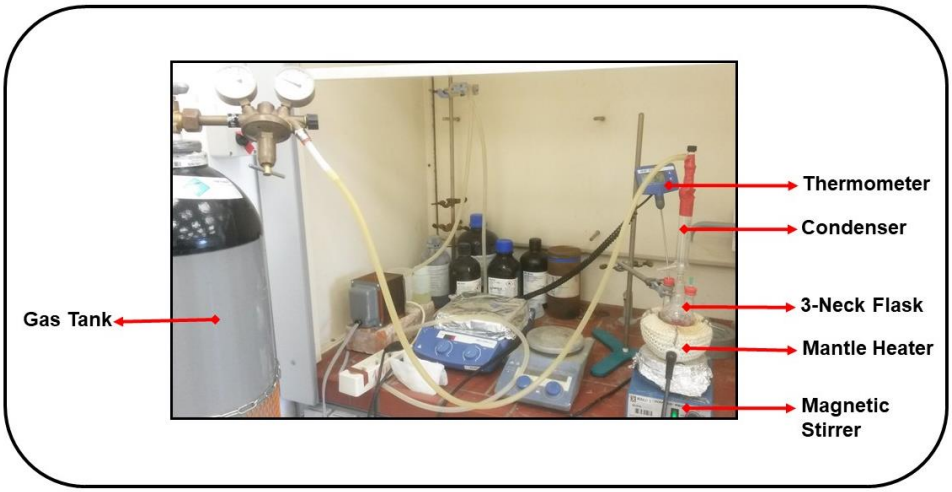


Figure 3.1 Synthesis setup of Mo and Pt NPs

3.3 Synthesis of Pt NPs

To synthesize Pt NPs, the same synthesis procedure of Mo NPs was followed with some modifications. 0.21 g (4.0 mmol) $Pt(C_5H_7O_2)_2$, 1 ml OA, 1 ml OLA and 25 ml ODE were dissolved in a preheated (100 °C) three-neck flask under Ar atmosphere by using a magnetic stirrer. After complete dissolution of $Pt(C_5H_7O_2)_2$, the temperature was increased to 230 °C over 15 min, and kept at that temperature for 60 min. During the reaction time there is a clear color conversion from light yellow to black, which is evidence for the formation of Pt NPs. After this step, the same procedures were carried out as with the Mo NPs synthesis. The amount of Pt obtained at the end of the synthesis was 0,135 g and dissolved in 2 ml $CHCl_3$, then filtered using 0.45 μm PTFE syringe filter.



Figure 3.2 Images taken during synthesis of NPs (a) pyrolysis, (b) precipitation of NPs in centrifuge tubes, (c) filtering with qualitative filter paper, (d) powder of Mo NPs

3.4 Cleaning of Graphite Substrates

Graphite substrates were sanded with P 500 sandpaper in a container filled with water to obtain relatively clean and smooth surfaces (see Fig. 3.3). Then, substrates were washed with deionized water and ethanol, then dried at 50 °C for 20 min. The drying step ensures that there are no solvent molecules left on/inside the graphite.



Figure 3.3 Images of graphite substrates and sandpaper a) before cleaning with sanding b) sandpaper c) after cleaning with sanding

3.5 Deposition of Mo and Pt NPs

The suspensions containing Mo and Pt NPs suspension were deposited using a spin coater onto the graphite substrates at 1000 rpm for 20s. In this way, thin films made of metallic NPs were obtained (see Fig. 3.4 for application scheme of spin coating process). A small part of the substrate was covered with a scotch-tape patch which prevented coating of the whole substrate surface. This was done to create contacts (e.g. glue wire).

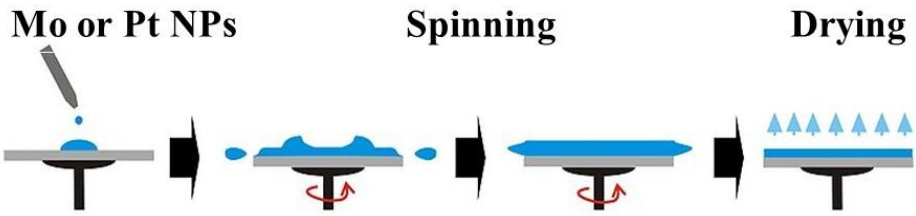


Figure 3.4 Spin coating application scheme [45]

3.6 Annealing of Textured Mo and Pt Catalysts

The obtained thin thin films of metallic NPs were placed in a tube oven and annealed at different temperatures (see Fig. 3.5). Before heating the thin films, the tube oven was purged with Ar (99.999%) for 30 min with 500 ml/h gas flow to remove oxygen inside the oven. During the heating process, the Ar gas flow was kept at 100 ml/h. Since the Mo NPs are sensitive to oxidation the tube was loaded with iron turnings which were used as an oxygen scavenger (see Fig. 3.6).

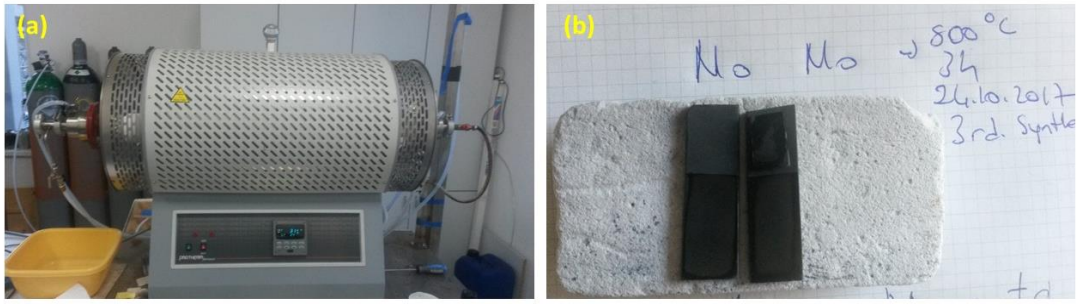


Figure 3.5 Images of (a) the utilized oven and (b) obtained Mo-based electrodes

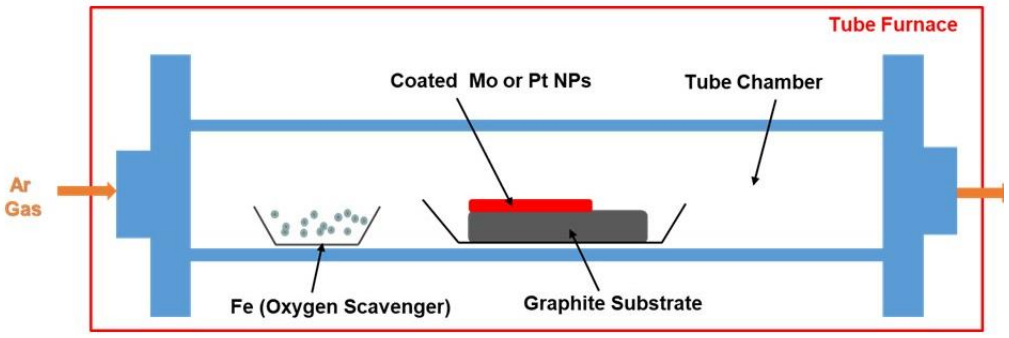


Figure 3.6 The annealing scheme of electrodes in the oven. Note: Iron turnings were not used at the annealing of Pt NPs

Mo thin films were annealed at different temperatures and times from 50°C to 1450°C under Ar (99.999%) atmosphere for 1h to 3h. Textured metallic Pt thin films were only annealed at 500 °C and 1000 °C for 3h. In this way, Mo- or Pt-based electrodes (samples) were obtained to use in HER. The detailed annealing temperatures, times and nomenclature of samples are shown in Table 3.1. The prepared electrodes will be named according to the nomenclature given in the Table 3.1 in the rest of the thesis.

Table 3.1 Annealing temperatures, times and nomenclature of Mo- and Pt-based electrodes

		Annealing Time (h)	Pt NPs	Nomenclature	Mo NPs	Nomenclature
Temperature (°C)	1450	3			✓	Mo-G1450
	1150	3			✓	Mo-G1150
	1000	3	✓	Pt-G1000	✓	Mo-G1000
	900	3			✓	Mo-G900
	800	3			✓	Mo-G800
	800	2			✓	Mo-G800-2h
	500	3	✓	Pt-G500	✓	Mo-G500
	300	1			✓	Mo-G300
	50	1			✓	Mo-G50

3.7 Attaching Electric Wires

Bare electric wires were connected by using silver paste to ensure electrical conductivity between the electrode and wires during measurements (see Fig. 3.7). The composition of each electrode before the electrochemical tests was studied using X-ray diffraction (XRD). Later the electric wires were attached to the electrode. After attaching the wires, electrodes were placed in a furnace at 40 °C to dry the silver paste.

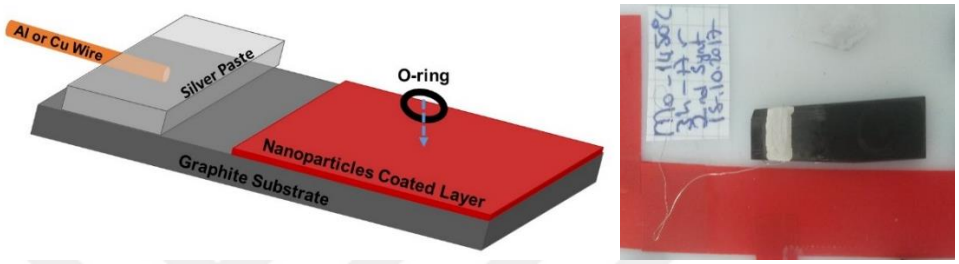


Figure 3.7 (a) Schematic and (b) real images of prepared electrodes

CHAPTER 4

4 CHARACTERIZATION METHODS

4.1 X-Ray Diffraction (XRD) Measurements

In this study, the phase composition of annealed Mo and Pt catalysts as well as the bare graphite electrode was determined by a Rigaku Miniflex 600 Powder X-ray Diffractometer (Fig. 4.1) operation with Cu Kα radiation (λ = 1.54 Å). The diffraction patterns were gathered over 10-80 ° with a step size of 0.02 °. Results were analyzed using PDXL software by comparing with known phases (PDF diffraction data files).



Figure 4.1 Rigaku Miniflex 600 Powder X-ray Diffractometer

4.2 Transmission Electron Microscopy (TEM)

The crystallinity and sizes of Mo and Pt NPs were investigated using a JEOL-2100 F system operating at 200 kV, equipped with an Energy Dispersive X-ray Spectroscopy (EDS) detector (Fig. 4.2). To prepare TEM samples, aliquot from Mo and Pt NPs suspension were taken and added drop-by-drop into a glass cup containing deionized water. Since, the NPs are hydrophobic they form a thin layer above the water surface. Then, a Cu grid which is commonly used in TEM was immersed into the aqueous solution and removed gently. Later, the Cu grid was placed in an oven at 50 °C for 5 to 10 min.



Figure 4.2 JEOL-2100 F Transmission Electron Microscopy setup

4.3 Scanning Electron Microscopy (SEM)

In this study, the morphology, composition and structure of the samples were studied with a Scanning Electron Microscope (SEM) (Jeol JSM 7100F) equipped with a field-emission electron gun and coupled to an Energy Dispersive Spectrometer (EDS) (Oxford Instruments) as shown in Fig. 4.3.

SEM combined with EDS studies is a powerful tool to investigate the morphology and composition of material at a micron and sub-micron level [46].



Figure 4.3 JEOL JSM-7100 F Scanning Electron Microscopy setup

4.4 Electrochemical Measurements

All electrochemical measurements were conducted using an EDAQ SP1 potentiostat in a three-electrode configuration. In this configuration, the potential is applied by the potentiostat to the working electrode and obtaining current is measured between working electrode and counter electrode. The potential is measured between reference and working electrode. In this study, prepared electrodes, a coiled Pt wire and an Ag/AgCl electrode were used as the working, counter and reference electrode, respectively, as shown in Fig. 4.4.

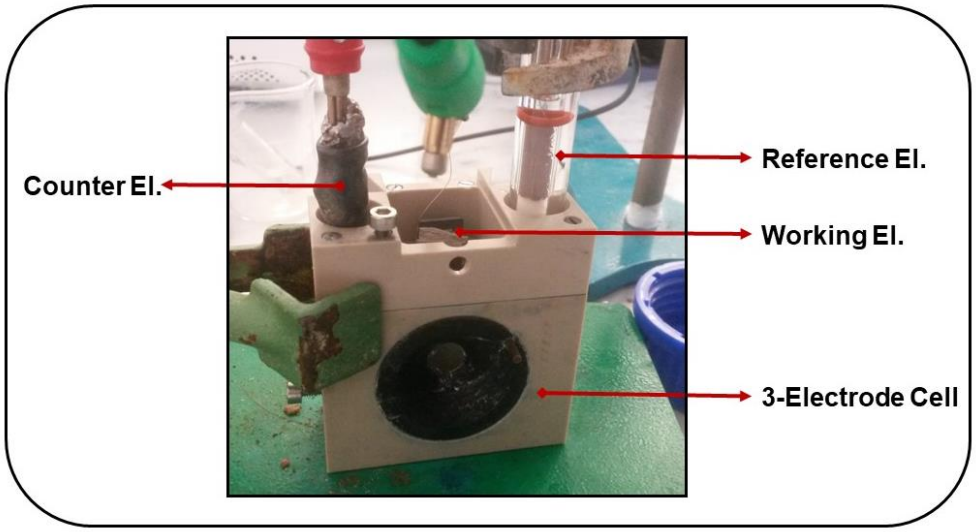


Figure 4.4 Three-electrode configuration and related electrodes

The electrocatalytic activity of prepared electrodes towards HER were investigated by using linear sweep voltammetry (LSV) technique in aqueous 0.5 M H_2SO_4 (pH = 0). Cyclic voltammetry (CV) techniques was also studied to check the stibility of the prepared electrodes. LSV and CV curves were obtained at a scan rate of 2 mV/s and 100 mV/s, respectively. During measurements, an O-ring was inserted between working electrode and sample holder to define the working area of the electrode as 0.283 cm^2. The obtaining currents *(I)* were converted to the current density *(j)* according to Eq. 4.1;

$$j = \frac{I}{0.283\ cm^2} \times 1000 \qquad \textbf{(4.1)}$$

where I and j are in A and mA/cm^2, respectively. The potential values of I-V data were referenced to reversible hydrogen electrode (RHE) with the help of Eq. 4.2:

$$E_{RHE} = E_{Ag/AgCl} + E^{\circ}_{Ag/AgCl} + 0.195 * pH \quad \textbf{(4.2)}$$

where E_{RHE} is the calculated potential versus RHE, and $E_{Ag/AgCl}$ is the measured potential vs Ag/AgCl and standard potential of Ag/AgCl ($E^{\circ}_{Ag/AgCl}$) $is\ 0.197\ V$ at room temperature [47].

4.5 Impedance Spectroscopy

The Electrochemical Impedance Spectroscopy (EIS) measurements were performed using a three-electrode configuration in 0.5M H_2SO_4 in the same manner as described in section 4.4. The measurements were done in a potentiostatic mode at various potentials from 0.0 to -0.3 V versus RHE in the frequency range of 0.01 to 10^6 Hz with an amplitude of 10 mV.

4.6 Stability Tests

The stability tests were performed in three-electrode configuration in aqueous 0.5 M H_2SO_4 electrolyte solution. We found that Pt easily corrodes in an acidic environment under applied potential generating Pt^{2+} ions. The latter ions can be electrochemically reduced to metallic Pt on the working electrode. Therefore, a two compartment cell with a Nafion membrane was employed for the stability tests. The Nafion membrane allows to pass only H^+ ions and prevent migration of Pt^{2+} ions.

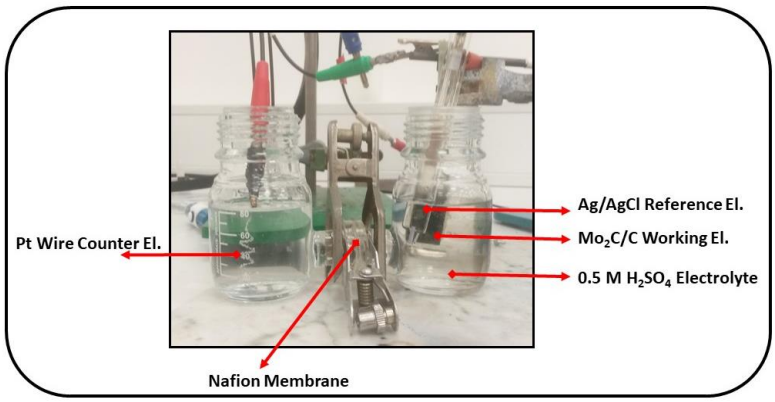


Figure 4.5 Three-electrode configuration with Nafion membrane and related electrodes

A mechanism was designed to carry out stability test as shown in Fig. 4.5. Two glass bottles polished in their lower opening part were joined and a Nafion membrane was inserted between these joints. The working and reference electrodes were placed in the same compartment while the Pt wire counter electrode was placed in the other compartment. Hence the Nafion membrane only allows H^+ ions to pass and prevents contamination of the working electrode with Pt^{2+} ions as well as erroneous measurements. To be able to define a geometric area, part of electrode surface was covered with a ClaroCit polymer/resin. To prepare the polymer, ClaroCit powder was mixed with ClaroCit liquid (1:2 weight ratio) and then quickly applied to the uncoated surfaces of the working electrodes as depicted in Fig. 4.6.

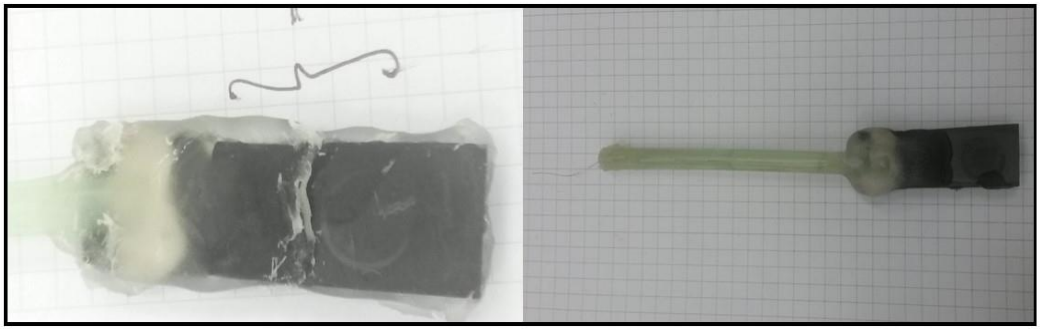


Figure 4.6 Image of prepared electrodes for stability test

For stability tests, 1000 CV cycles were done between -0.2 and -0.8 V with a scan rate of 100 mV/s to the Mo-G800 and Mo-G900 samples in 0.5M H_2SO_4 at room temperature. In Fig.4.7, hydrogen generation by Mo-G800 sample is shown.

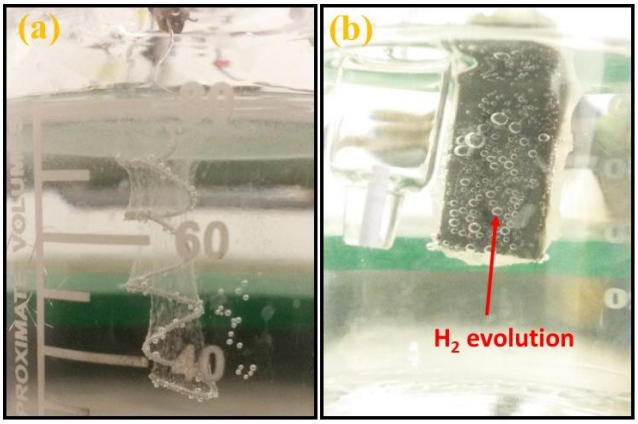


Figure 4.7 (a) O_2 generation at Pt wire counter electrode (anode), (b) H_2 generation at prepared working electrode (cathode) during stability test of Mo-G800 sample.

CHAPTER 5

5 RESULTS AND DISCUSSIONS

5.1 XRD Pattern of Bare Graphite

Fig. 5.1 (a) shows the XRD pattern of bare graphite substrate. Diffraction peaks present at 2θ values of 42.2°, 44.3°, 54.1°, 59.96° and 77.4° indexed to the (100), (101), (004), (004) and (103) planes (PDF Card:1011060). The absence of other peaks indicates that the graphite is of high purity. The crystallinity of as-synthesized Pt NPs was also studied by XRD. The synthesized Pt NPs demonstrate the typical cubic structure ($Fm\bar{3}m$ (225)) (PDF Card: 1011107) as shown in Fig. 5.1 (b) After purification the obtained Pt NPs were spin-coated onto graphite substrates.

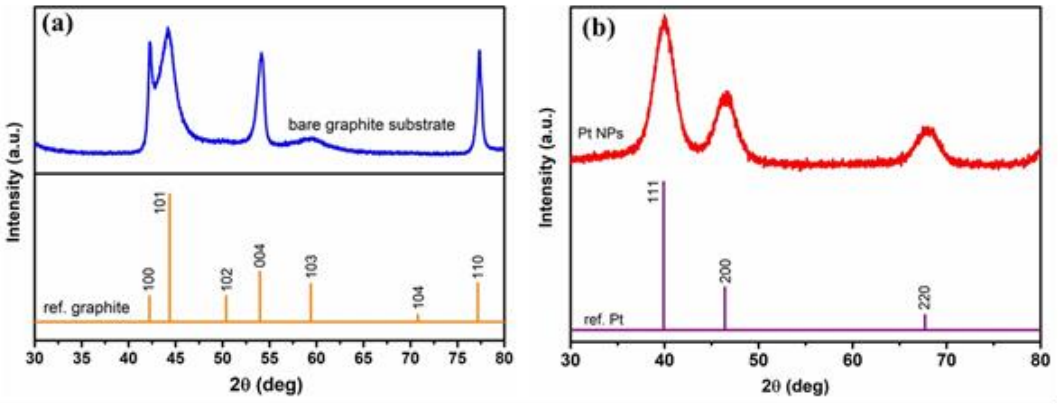


Figure 5.1 XRD pattern of (a) bare graphite substrate and (b) synthesized Pt NPs

5.2 XRD Pattern of Pt-based Electrodes

Fig. 5.2 shows diffractograms of Pt NPs on graphite substrate heat treated at 500 and 1000 °C. The samples (electrodes) are abbreviated as Pt-G500 and Pt-G1000. The peaks at around 40° and 46.4° of both Pt-G500 and Pt-G1000 samples are ascribed to the diffraction of the (111) and (100) planes of Pt (PDF Card: 1011107), respectively. The difference of peak intensities can be attributed to different amounts of Pt loading onto the graphite substrates.

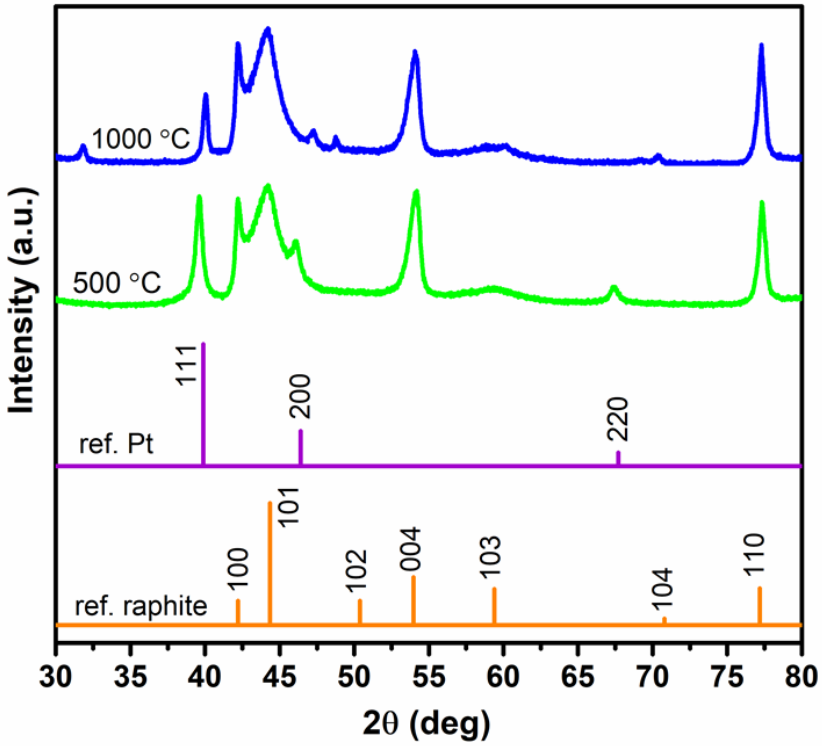


Figure 5.2 XRD pattern of Pt-based electrodes heat-treated at 500 °C and 1000 °C

5.3 XRD Pattern of Mo NPs

Fig 5.3 shows XRD diffractogram of as-synthesized Mo NPs deposited on a special glass holder. The broad peak of the Mo sample at ~26° matches with the diffraction pattern of the glass holder. Therefore, it can be concluded that synthesized Mo NPs have an amorphous structure. Structural characterization of Mo NPs will be proven below in section 5.6.

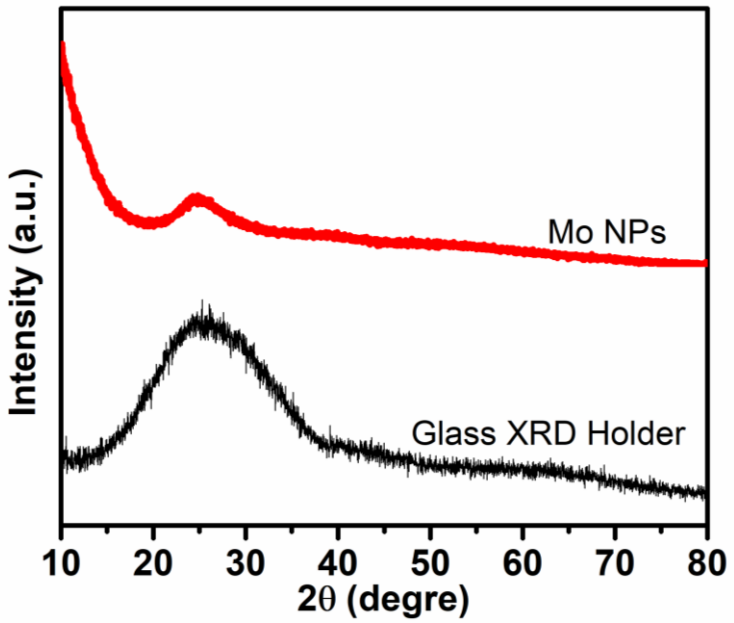


Figure 5.3 XRD pattern of as-synthesized Mo NPs

5.4 XRD Pattern of Mo-based Electrodes

Figure 5.4 shows Mo-C phase diagram that varies with temperature and carbon ratio. The analyzed crystal structures of Mo-based electrodes by using X-ray diffraction data were confirmed according to the Mo-C phase diagram. [48].

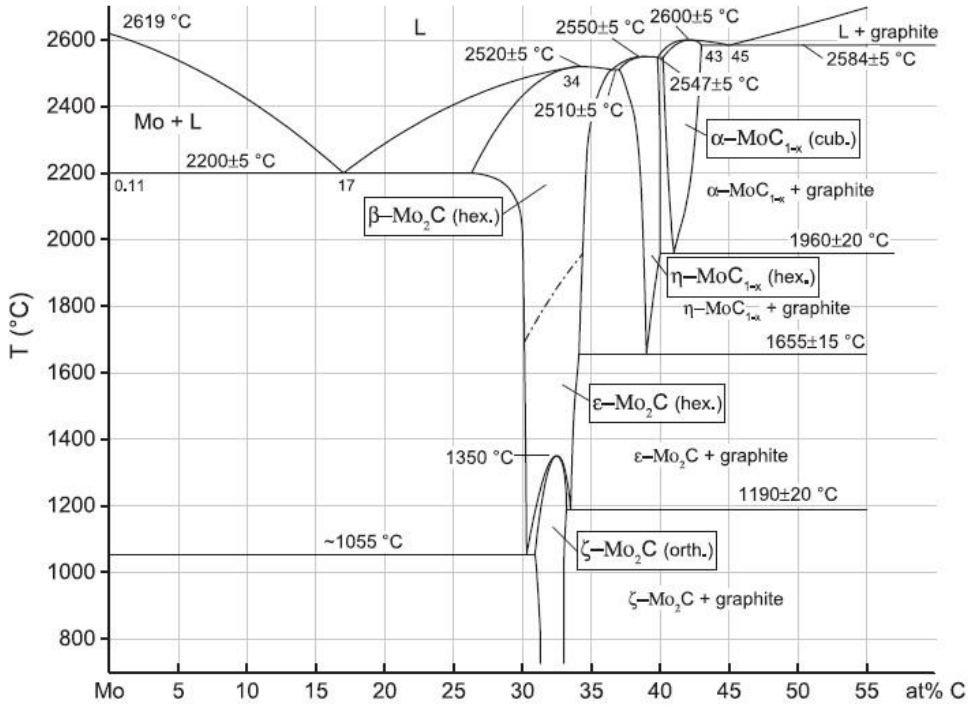


Figure 5.4 Phase diagram of Mo-C [48]

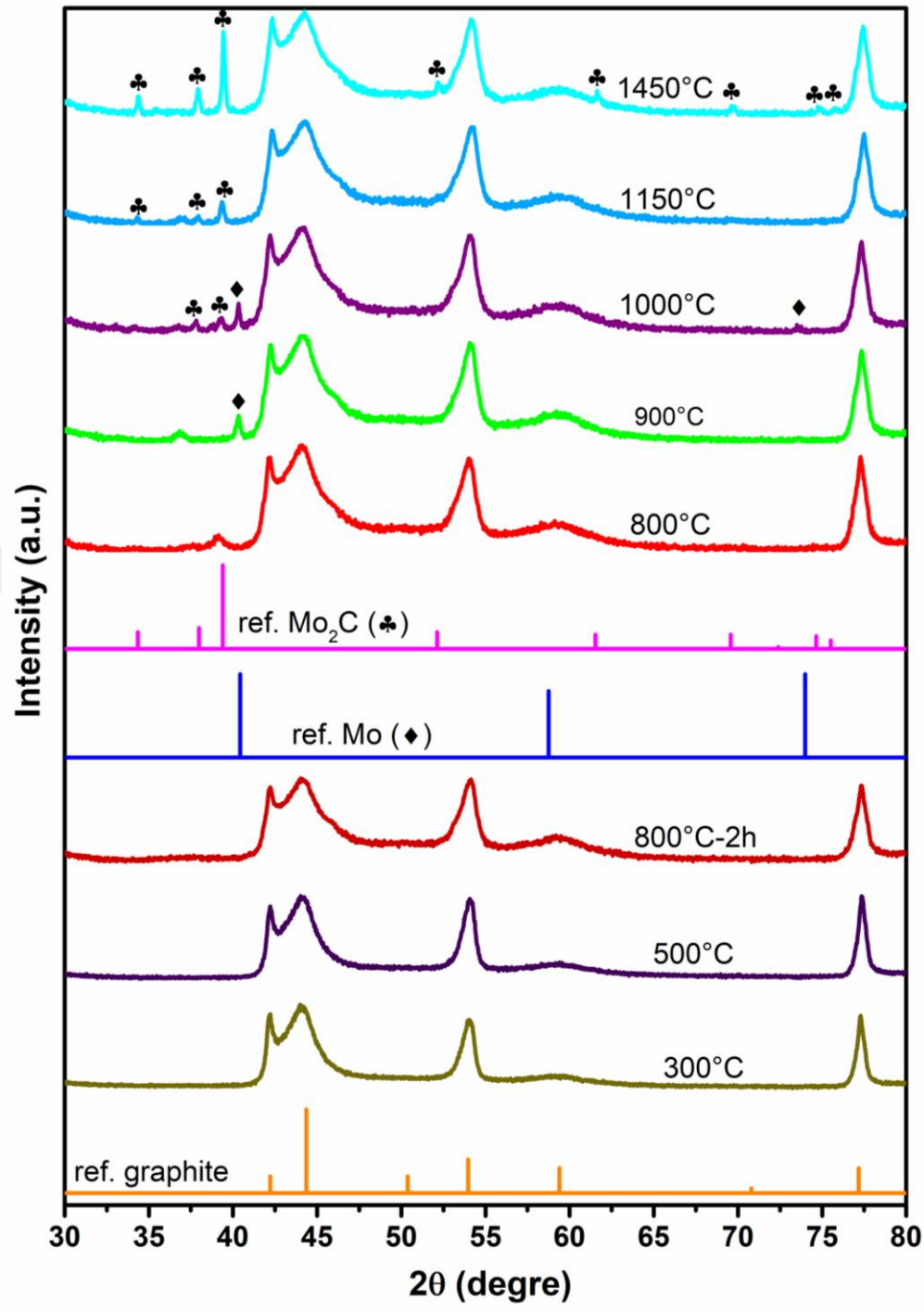


Figure 5.5 XRD pattern of Mo-based electrodes heat treated at different temperatures from 300 to 1450 °C

Fig 5.5 depicts XRD diffraction patterns of Mo-based electrodes heat treated at different temperatures on graphite substrate. All Mo-based electrodes show diffraction peaks at 2θ=42.21°, 44.36°, 53.97°, 59.4° and 77.18° which correspond to standard diffraction peaks of graphite (PDF Card:1011060). The electrodes which

heat treated below 800 ºC do not show any diffraction peaks for typical Mo phases. Heating at 800 ºC for 3h causes crystallization of amorphous Mo NPs to cubic metallic Mo (PDF Card: 00-001-1205). The sample heat treated at 1000 ºC contains both metallic Mo phase and hexagonal Mo_2C (P63/mmc (194), CAS 12069-89-5). The diffraction peak at 40.33° is attributed to cubic metallic Mo (PDF Card:00-001-1205). Heating the electrodes to 1450 ºC yields pure hexagonal Mo_2C phase [49].

5.5 TEM Images of Pt NPs

High-resolution transmission electron microscopy (HRTEM) images of synthesized Pt NPs are given in Fig 5.6. The average size of Pt NPs is on the order of 4 nm. The electron diffraction image shown in Fig. 5.6 (f) is a proof of the crystallinity of Pt NPs.

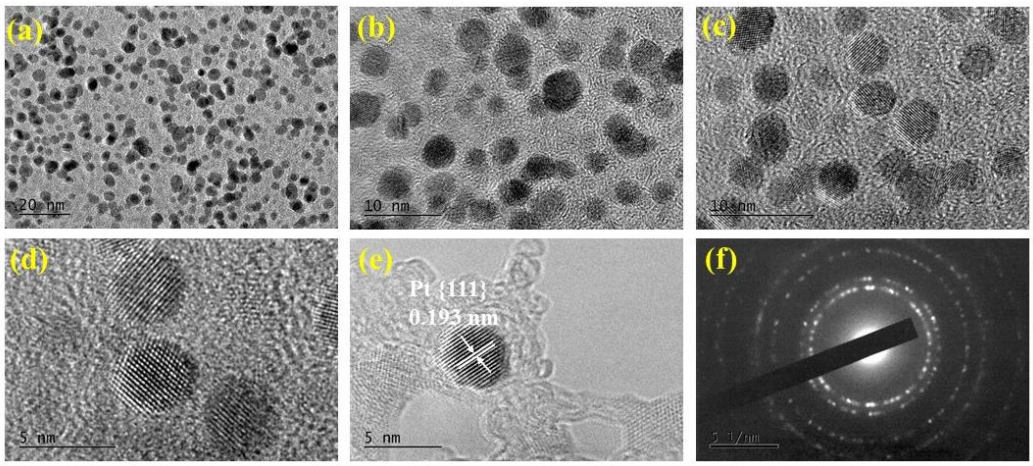


Figure 5.6 (a), (b), (c) TEM) and (d), (e) HRTEM images of Pt NPs. (f) Electron diffraction image of Pt NPs. Scale bars are (a) 20 nm, (b), (c) 10 nm, (d) and (e) 5nm, respectively

High Resolution Transmission Electron Microscope (HRTEM) images show that the Pt NPs are single crystals enclosed by (111) and (200) crystal planes (Fig. 5. 6 (c), (d)). The distance between two Pt lattice fringes is 0.193 nm, close to the distance of Pt (111) planes (0.196 nm) in a face-centered cubic (fcc) Pt crystal ($Fm\bar{3}m$ (225)).

5.6 TEM Images and EDS Maps of Mo NPs

The TEM images of Mo NPs shown in Fig. 5.7 demonstrate that synthesized Mo NPs have small particle sizes (≤ 5 nm). As expected the small crystallites are amorphous.

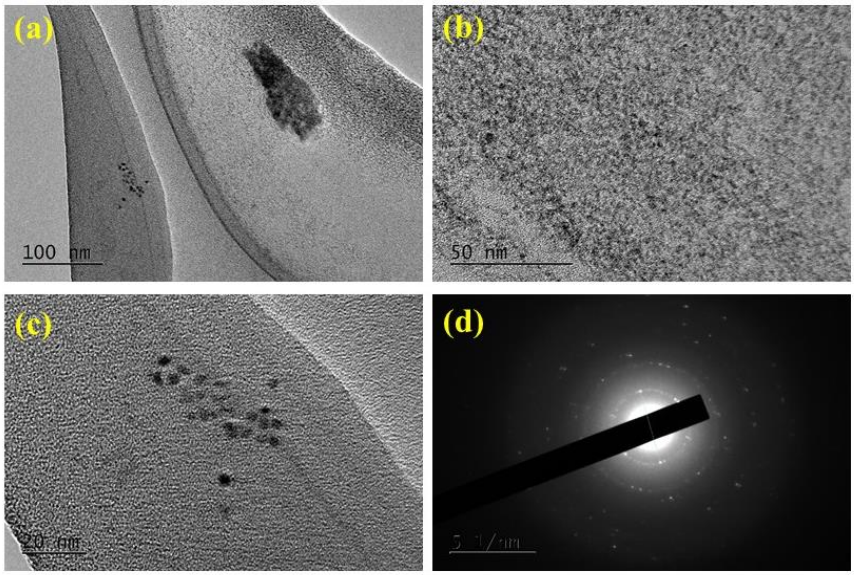


Figure 5.7 TEM (a, b, c) images of Mo NPs at different magnifications. (d)Electron diffraction image of Mo NPs. Scale bars are (a) 100 nm, (b) 50 nm, (c) 20 nm

Fig. 5.8 shows the TEM image and corresponding elemental distribution maps of Mo, C and O taken from a polymeric grid coated with Mo NPs. It can be concluded that Mo NPs are uniformly dispersed on the polymeric membrane. The presence of O and C signals can be associated with the polymer membrane and also with the molecules (e.g. OLE and OA) which most probably cover the surface of Mo NPs.

EDS elemental spectrum of synthesized Mo NPs has a high intense peak at around 2.15 keV which proves that Mo NPs were synthesized successfully as shown in Fig. 5.8 (e). The Mo NPs suspension contains no Si based material, therefore the small Si peak at 1.7 keV might originate from a contaminant.

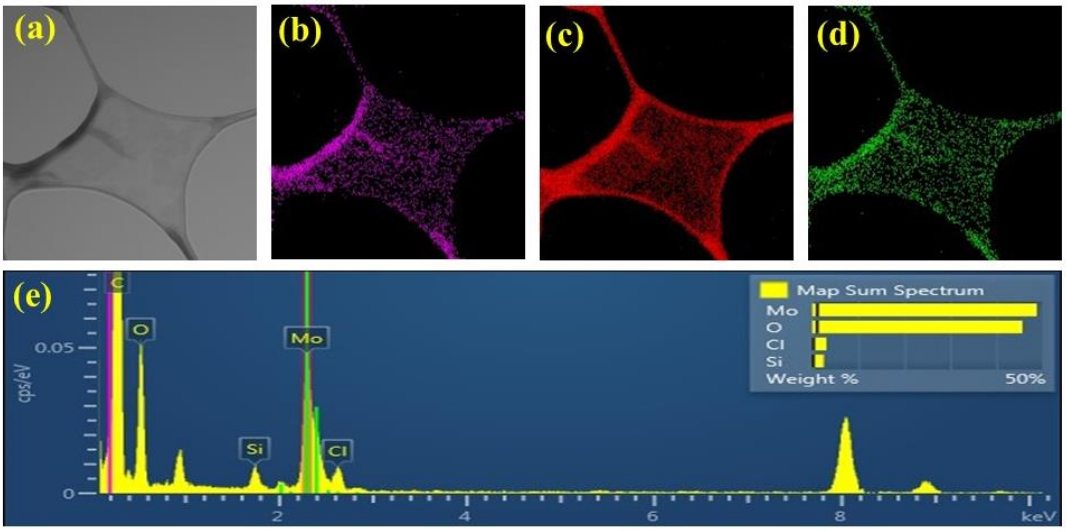


Figure 5.8 TEM image of synthesized Mo NPs. The corresponding elemental mapping of (b) Mo, (c) C, (d) O. (e) The corresponding elemental spectrum of Mo NPs.

5.7 SEM Images of Bare Graphite Substrate

Fig. 5.9 (a), (b) and (c) show SEM images of the surface of bare graphite substrate. The surface of the graphite is relatively smooth with few holes in it. As depicted in Fig. 5.9 (e) and (f), the internal morphology of graphite substrate is composed of layered sheets which allows good coverage and anchoring of NPs. Moreover, the layered sheets also increase the contact surface between the liquid electrolyte and the loaded metallic NPs (e.g. Mo an Pt), thus facilitates chemical reactions. The reasons for using graphite as a substrate are as follows:

I. Graphite serves as a carbon source to provide in-situ conversion of metal NPs to metal carbides and composites at high temperatures. It reduces the cost for fabrication of metal carbide catalyst without using any reducing gases (e.g. H_2 and CH_4).
II. It is well-known that carbon has very good electrical conductivity, thus can be used to fabricate conductive electrodes.
III. Graphite can be processed at high temperatures and also it is an inexpensive material.

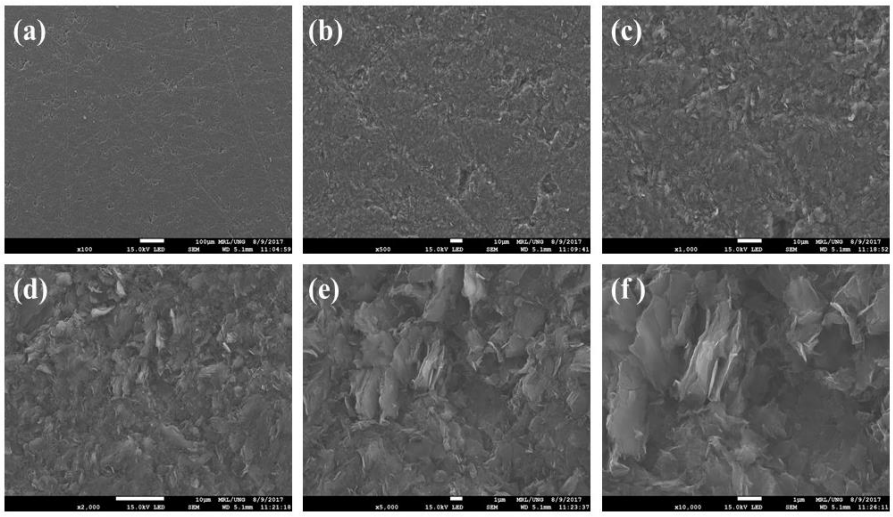


Figure 5.9 SEM images of bare graphite substrate at different magnifications. Scale bars are (a) 100μm, (b), (c), (d) 10μm, (e) and (f)1μm, respectively

5.8 SEM Images of Pt-based Samples

SEM images of the Pt-G500 sample annealed at 500 °C on graphite substrate are shown in Fig. 5.10. This sample contains small Pt NPs and also large formations. Within the squares, we show a hexagonal Pt structure which is 10 μm in size. (Fig. 5.10 (c), (e), (f)).

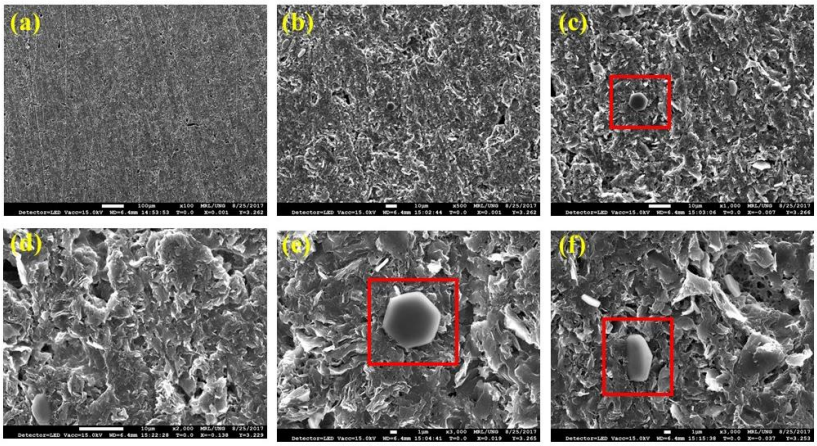


Figure 5.10 SEM images of Pt-G500 sample at different magnifications. Scale bars are (a) 100μm (b), (c), (d) 10μm (e), (f) 1μm. Red squares define hexagonal structured Pt

Fig. 5.11 presents SEM images of the Pt-G1000 sample at different magnifications. The Pt NPs annealed at 1000 °C form significantly rod-like structures as indicated

within red-dotted circles in Fig. 5.11 (c). During heat treatment at 1000 °C the Pt crystallites undergo the so-called Ostwald ripening process. The length of these rod-like structures are in the order of several micrometers while their thickness is about 1 μm in diameter. The small sizes of Pt structures yield high catalytic activity. Indeed, the Pt-G1000 sample shows relatively high catalytic activity towards HER (see section 5.13).

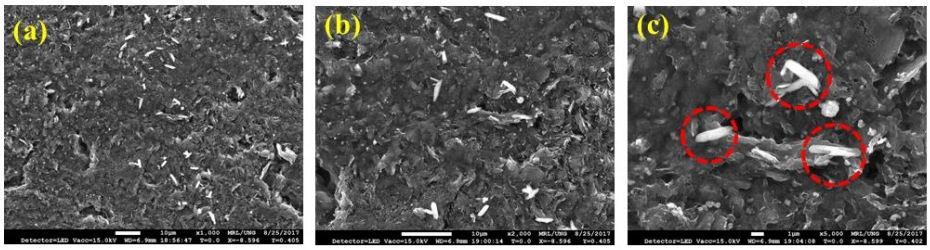


Figure 5.11 SEM images of Pt-G1000 sample at different magnifications. Scale bars are (a) 10μm (b) 10μm (c) 1μm. Red dotted circles show rod-like structure

5.9 SEM Images and EDS Maps of Mo-G800 Sample

Fig. 5.12 displays SEM images of the Mo-G800 sample obtained by heat treatment of Mo NPs-coated graphite substrate at 800 °C for 3h. It is clearly seen that the graphite surface is densely coated with a layer of Mo NPs (Fig. 5.12 (b)). There is a negligible agglomeration, which commonly occurs at high temperatures. In addition to the growth of larger (~100 nm) formations there are also small nanoplatelets which grow on the film (Fig.12 (d)). The sizes of these nanoplatelets vary from 20 to 100 nm.

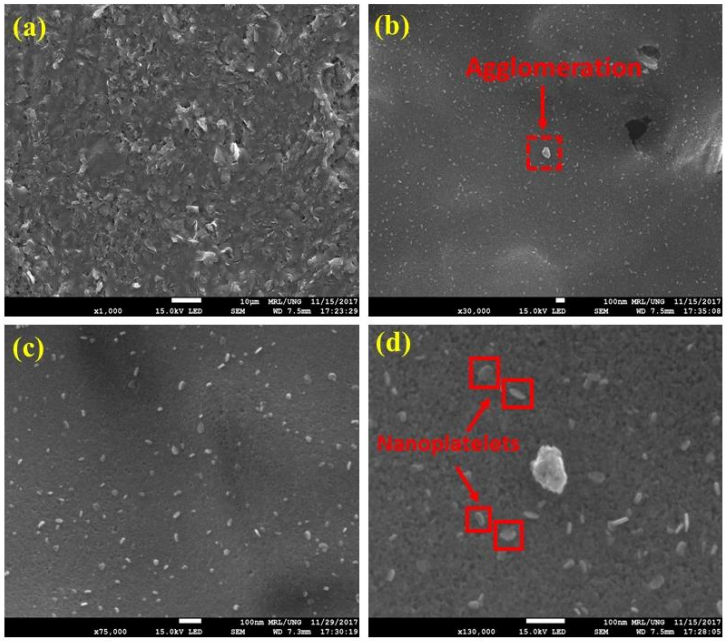


Figure 5.12 SEM images of Mo-G800 sample at different magnifications. Scale bars are (a) 10μm, (b) 100nm, (c) 100nm, (d) 100nm

A SEM image and corresponding EDX elemental maps of the Mo-G800 sample are shown in Fig 5.13. The figure reveals that Mo is homogeneously distributed on the surface of the graphite electrode. C signal comes from graphite substrate which is used both as a carbon source and substrate (Fig. 5.13 (c)). On the other hand, the signal/distribution of O is not even. The presence of the O signal could be due to adsorbed O_2 or the presence of molybdenum oxide in the surface layer. Indeed, in the XRD diffractograms for some samples we have seen the formation of small quantities of molybdenum oxide (MoO_x, x=0÷3). To prevent the formation of an oxide layer the tube oven, used during synthesis, must be purged long enough (30 min, 500 ml/h) with Ar gas before the heat treatment step. Adding sufficient quantities of Fe pieces, an oxygen scavenger, can also be a way to overcome the oxidation of Mo NPs.

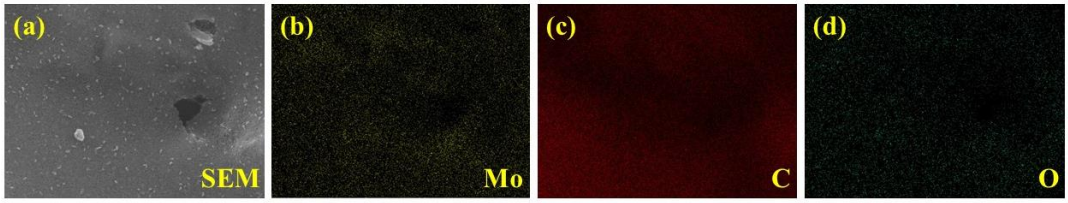


Figure 5.13 SEM image and corresponding EDS mapping of Mo-G800 sample

5.10 SEM Images of Mo-based Samples Prepared at 900, 1000 and 1150 °C

Fig 5.14 displays SEM images of Mo NPs coated on graphite substrate and annealed at 900, 1000 and 1150 °C for 3h (Mo-G900, Mo-G1000, Mo-G1150 samples) at two magnifications. Obviously, Mo NPs begin aggregation above 800 °C, thus inducing structures that do not have well defined shapes as seen in Fig. 5.14. It can be concluded that by increasing the temperature the formations become bigger. SEM images of samples annealed at 800, 900, 1000 and 1150 °C and the average particle sizes of Mo-based phases are depicted in Fig. 5.15. Apparently, as seen in the figure, the average particle size increases with increasing temperature. Typical sizes of Mo aggregates in the Mo-G800, Mo-G900, and Mo-G1000 samples are in the range of <30 nm, <200 nm, <500 nm and <900 nm, respectively.

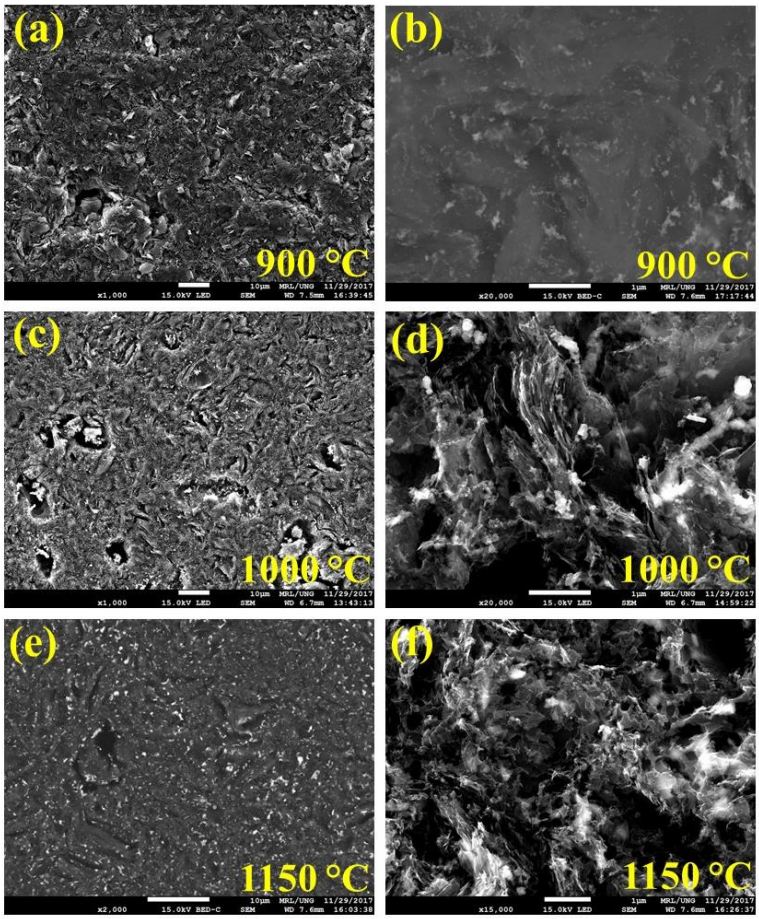


Figure 5.14 SEM images of Mo-based samples heat-treated at 900, 1000 and 1150 °C. Scale bars are (a), (c), (e) 10μm and (b), (d), (f) 1μm

The particle size is one of the most important parameters for electrocatalytic activity, since catalytic activity towards HER of samples decrease with increasing particle size as displayed in section 5.14. Notably, Mo-G800 sample shows the highest catalytic activity while Mo-G1150 sample shows the lowest activity among these four samples. Most probably the samples with smaller sizes exhibit the highest surface area.

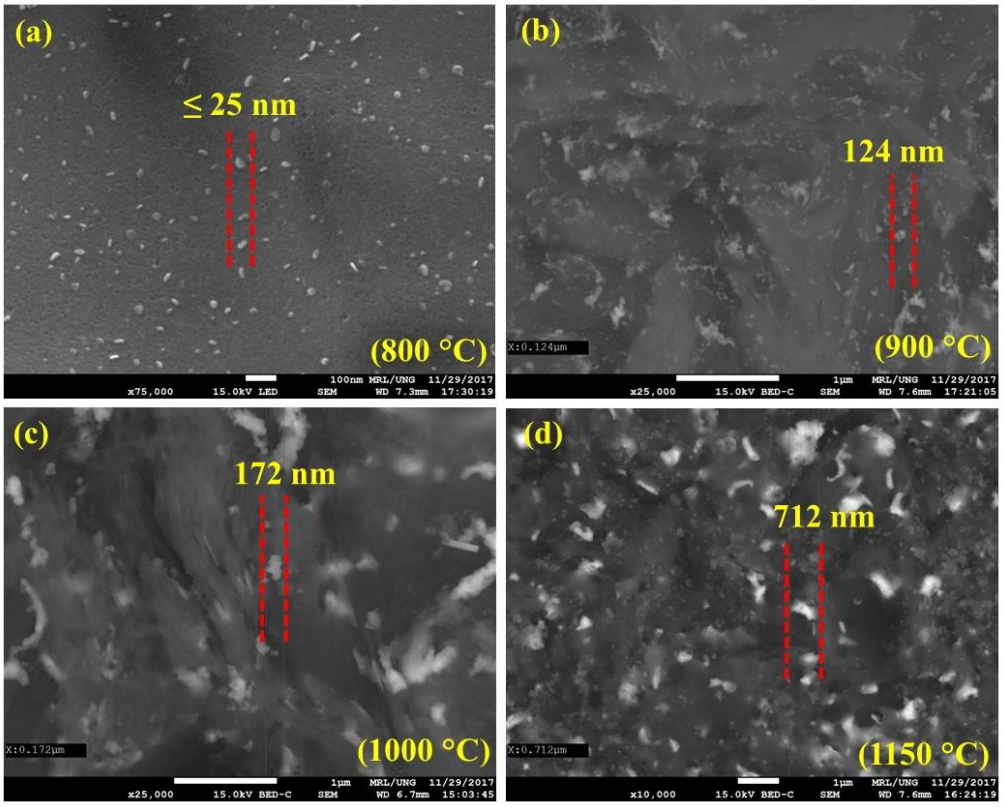


Figure 5.15 SEM images of Mo-based samples heat-treated at (a) 800, (b) 1000, (c) 1150 and (d) 1150 ° Scale bars are (a) 100 nm (b), (c), (d) 1 µm. Red dotted lines indicate corresponding particle size.

Fig. 5.16 shows SEM images and elemental maps of Mo-G900, Mo-G1000, and Mo-G1150 samples. The elemental analysis verifies that Mo NPs uniformly cover the graphite substrates. While in the Mo-G900 sample the Mo signal is evenly distributed, in the Mo-1150 sample the formation of larger aggregates is seen. Moreover, the EDS data also proves that the white spots in the SEM images are actually Mo or Mo_2C formations.

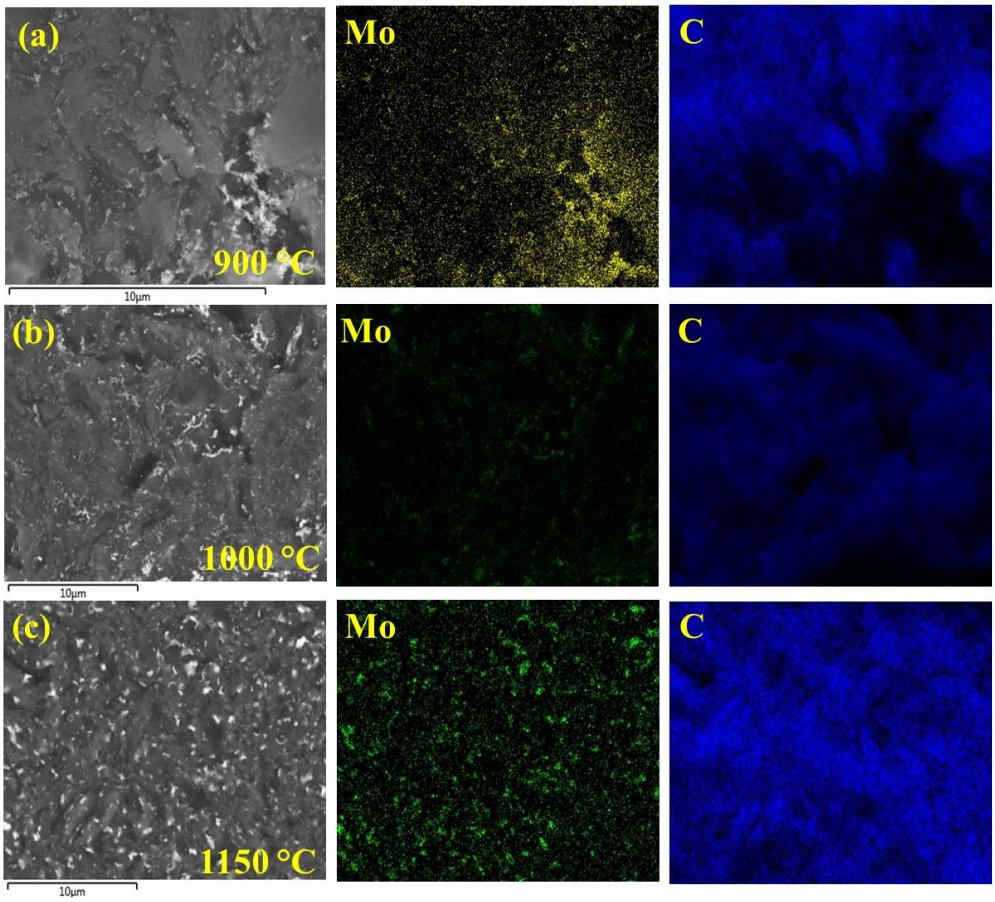


Figure 5.16 SEM image of Mo-based samples heat-treated at (a) 900, (b) 1000 and (c) 1150 °C and corresponding elemental mapping spectrums. Scale bars are (a), (b), (c) 10μm

5.11 CV Curve of Mo-G800 Sample

A cyclic voltammetry curve of the Mo-G800 sample in the potential range of 1.1 to -0.7 V in 0.5 M H_2SO_4 is shown in Fig. 5.17. In the forward scan, a cathodic reduction reaction of H^+ ions happens after -0.3 V. In the forward scan, between -0.2 to 1.1V we do not see any significant increase in current density which suggests that the sample is stable. The lack of any peak means that Mo film is not prone to oxidize. Also, as will be shown in a later section this sample exhibits low overpotential for HER.

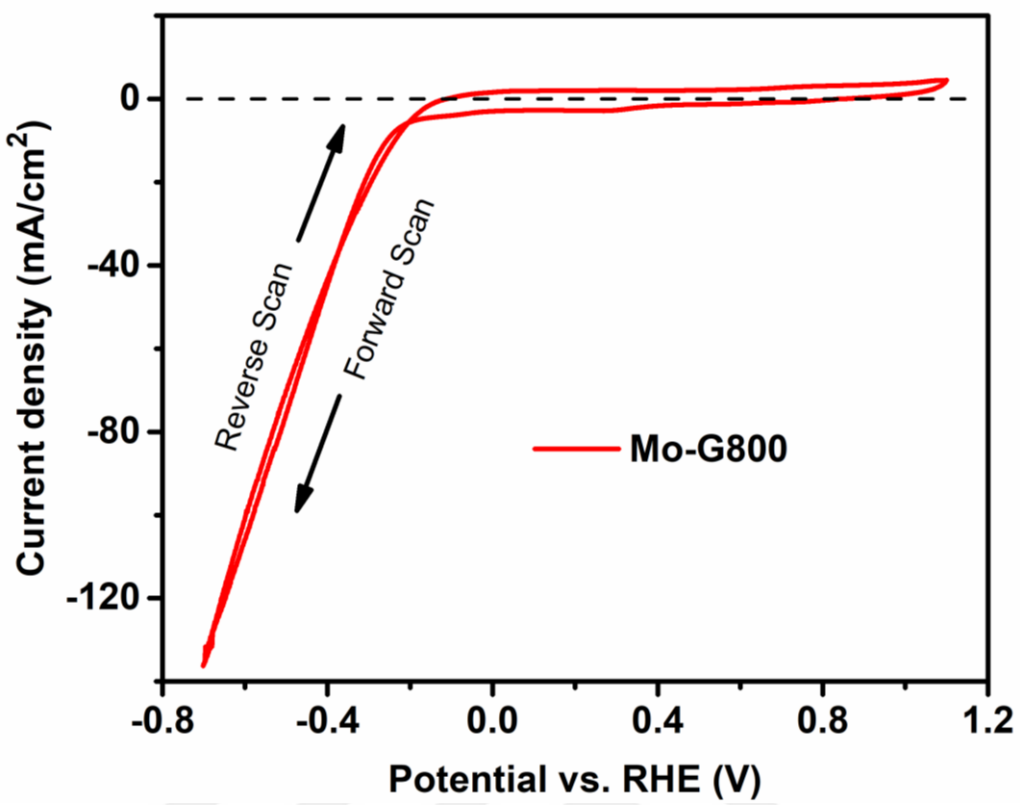


Figure 5.17 CV of Mo-G800 sample recorded in 0,5 M H_2SO_4 at a scan rate of 100 mV/s

5.12 CV Curves of Mo-G900 Sample

Fig. 5.18 shows CV curves of the Mo-G900 sample obtained after annealing of Mo NPs on graphite substrate for 3h at 900 °C. The electrode was cycled several times to clean its surface of a possible oxide layer (Fig 5.18 (b), (c)). After two cycles, the unwanted peaks disappeared and in the third cycle it gave a clear smooth voltammogram. At the potential of -0.7 V, the Mo-G800 sample gave a current density of 135.8 mA/cm^2 (see Fig. 5.17), while the Mo-G900 sample gave 102.6 mA/cm^2. This reveals that, the Mo-G800 sample has higher catalytic activity towards HER than the Mo-G 900 sample at high potentials.

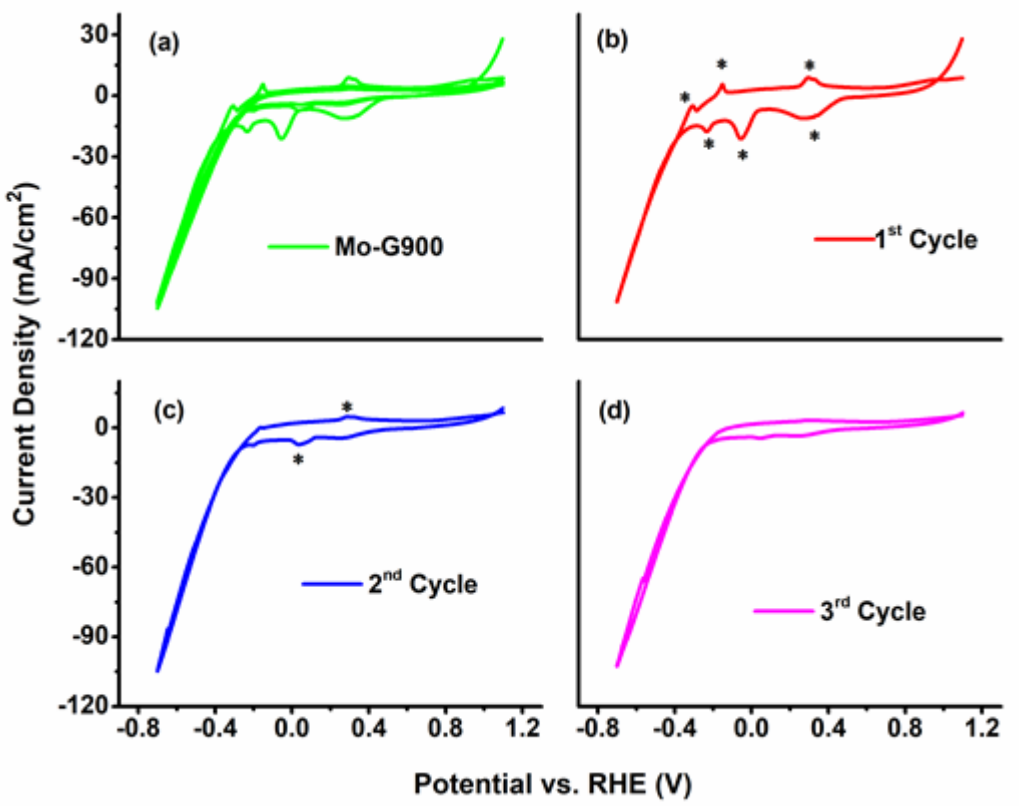


Figure 5.18 CV curves of Mo-G900 sample recorded in 0,5 M H_2SO_4 at scan rate of 100 mV/s.(a) Overlay of first 3 cycle (b), (c) and (d) 1st, 2nd and 3rd cycles, respectively. Asterisks show the peaks that arose from unwanted impurities on the electrode surface.

5.13 LSV Curve of Pt-based Electrodes and Bare Graphite Substrate

Fig. 5.19 shows LSV curves for Pt-G500 and Pt-G1000 samples. In the literature, overpotential (η_{10}) is defined as that required to drive 10 mA/cm^2 (j_{10}) current density. According to this, Pt-G500 and Pt-G1000 samples exhibit excellent catalytic activity with an onset potential (onset potential (η_0) is the potential required to drive current density of 1 mA/cm^2) 74 and 39 mV, respectively. The overpotential of the Pt-G500 and Pt-G1000 is 110 and 80 mV, respectively. Although both Pt samples exhibit excellent catalytic activity, the Pt-G1000 sample is preferred because of its higher catalytic activity. It is worth mentioning that the bare carbon electrode exhibited a negligible catalytic activity which required an overpotential of 800 mV to achieve a current density of 2.83 mA/cm^2 as shown in the inset of Fig. 5. 19. The active component in obtained Mo- and Pt-based samples is not the bare graphite substrate.

Based on these results, our Pt samples have high catalytic activity towards HER with negligible contribution from the bare graphite electrode. We used the Pt-G1000 sample as a reference material to compare with Mo samples.

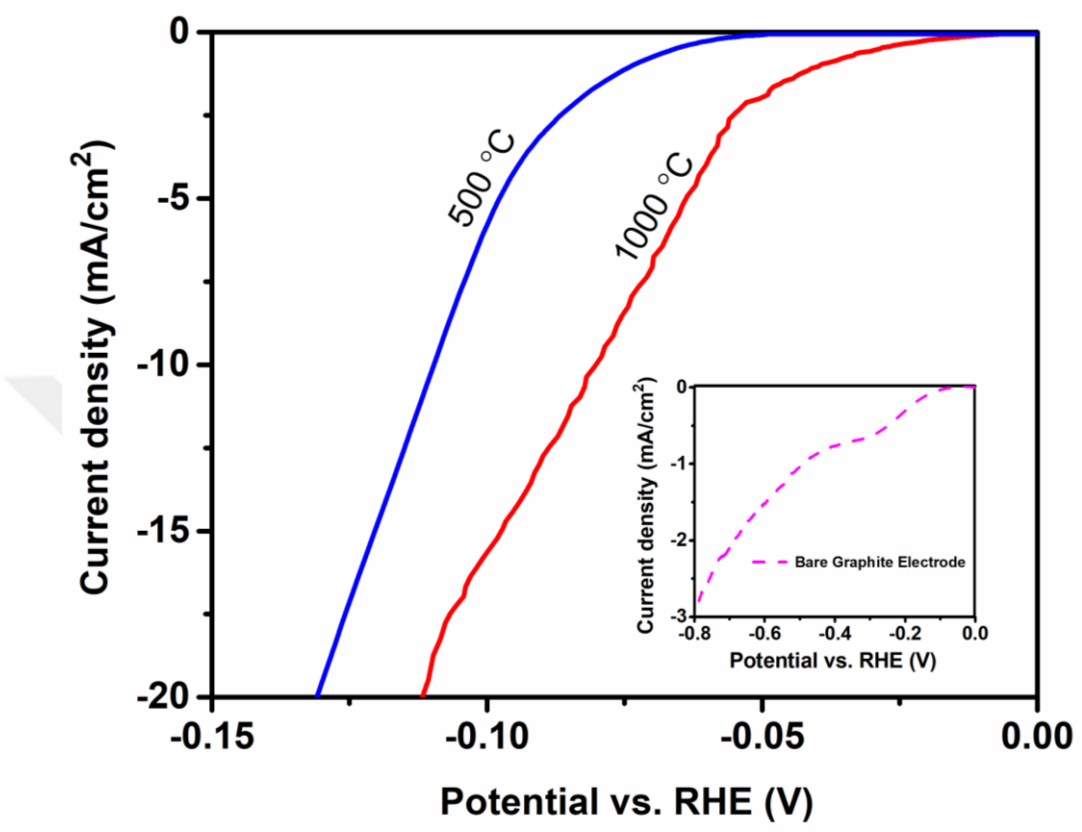


Figure 5.19 LSV curves of Pt-based electrodes recorded in 0,5 M H_2SO_4 at a scan rate of 2 mV/s. The inset is LSV curve of the bare graphite electrode without any heat treatments

5.14 LSV Curves of Mo-based Electrodes

LSV curves of Mo-G50, Mo-G300 and Mo-G500 samples are presented in Fig. 5. 20. We found that the Mo samples heat treated up to 800 °C contain only amorphous phase Mo (see XRD data). The Mo-G50 sample which was annealed at 50 °C for 1h yields negligible current density on the order of tens of μA as shown in Fig. 5. 20 and its inset. Specifically, residual organics such as ODE, OLA, and OA prevent the catalytic activity of Mo-G50 samples. Moreover, organics like ODE, OLA and OA have boiling points exceeding 270 °C. Therefore, residual solvents start to evaporate only at elevated temperatures. We can expect that at 500 °C the organic molecules will burn and produce carbon under an inert Ar atmosphere. Hence Mo-based

samples begin to show high catalytic activity towards HER. The overpotentials at 10 mA/cm^2 for Mo-G300 and Mo-G500 samples are 755 mV and 584 mV respectively. The Mo samples heat treated at 300 and 500 °C are an amorphous metallic phase since those temperatures are not enough to obtain crystalline metallic phase Mo or Mo_2C phase as demonstrated in the XRD plots.

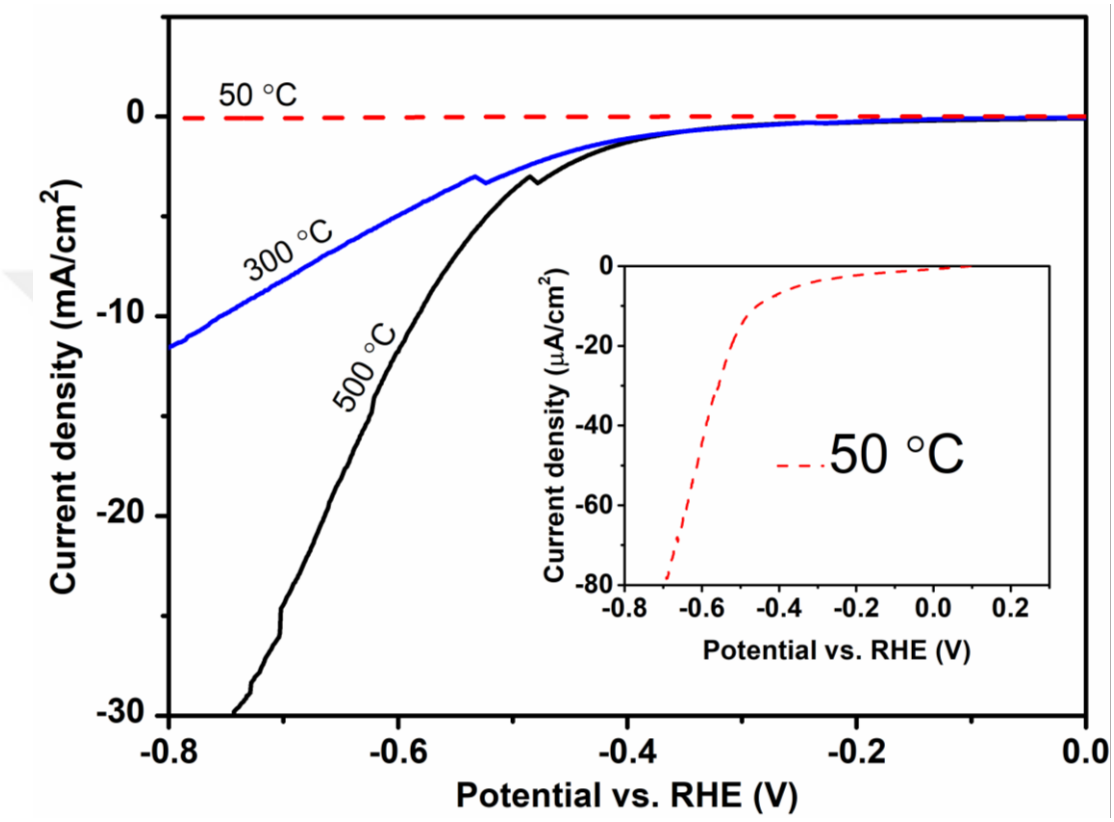


Figure 5.20 LSV curves Mo-based electrodes in 0.5M H_2SO_4 recorded with a scan rate of 2 mV/s. The inset is LSV curve of Mo-G50 sample

The LSV curves of Mo-based electrodes heat treated at different temperatures are shown in Fig. 5.21. From the overpotential values, we can see that the Mo-G800 sample shows the highest electrocatalytic activity for HER. It requires only 270 mV overpotential to drive 10 mA/cm^2 current density. In contrast, the η_{10} of Mo-G800-2h is 466 mV. It is worth mentioning that heat treatment at 800 °C does not yield Mo_2C but instead the amorphous phase Mo is prevalent. Most probably the cause for the improved overpotential in Mo-G800 (3h) could be due to better connectivity between the Mo grains, or improvement in the adhesion of Mo film to the graphite substrate. The onset and overpotential values of the rest samples are given in Table

5.1. It is clear that the overpotential obtained from the samples heat treated above or at 1000 °C is not suitable to achieve good catalytic activity towards HER. Although the Mo-G1000 sample has a 386 mV overpotential, this value is much higher than those of Mo-G800 and Mo-G900.

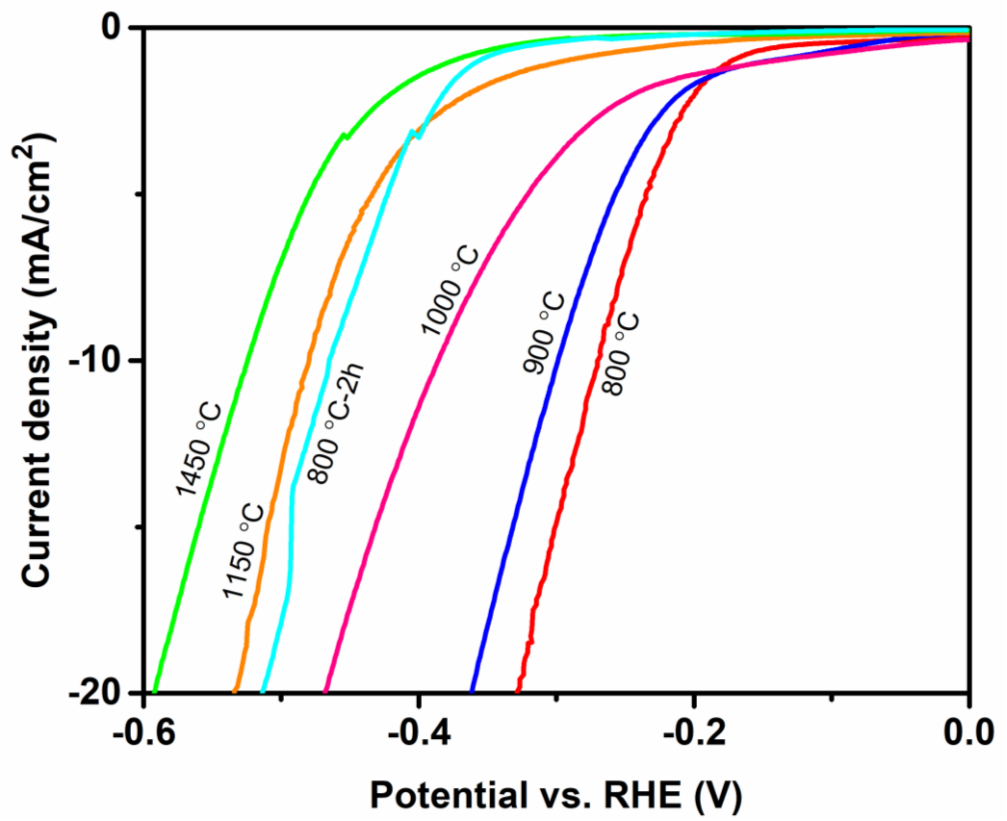


Figure 5.21 LSV curves of Mo-based electrodes in 0.5M H_2SO_4 recorded with a scan rate of 2 mV/s

5.15 Tafel Slopes of Prepared Electrodes

Fig. 5.22 shows Tafel plots calculated from the LSV measurements that were used to investigate HER kinetics. As shown in Fig. 5.22, the Pt-G1000 sample exhibits a Tafel slope of 30 mV per decade, which was found to be identical with previously reported values elsewhere for Pt [50, 51] and this proves the validity of our results. Mo-G800 and Mo-G800-2h samples give Tafel slopes of 71 and 91 mV per decade, respectively. It is expected that the HER process in these two samples proceed by a Volmer-Heyrovsky mechanism. Also, Mo-G800 sample exhibits the lowest Tafel slope amongst our Mo-based electrodes, which is consistent with the LSV data. A lower Tafel slope relates to higher electrocatalytic activity towards HER.

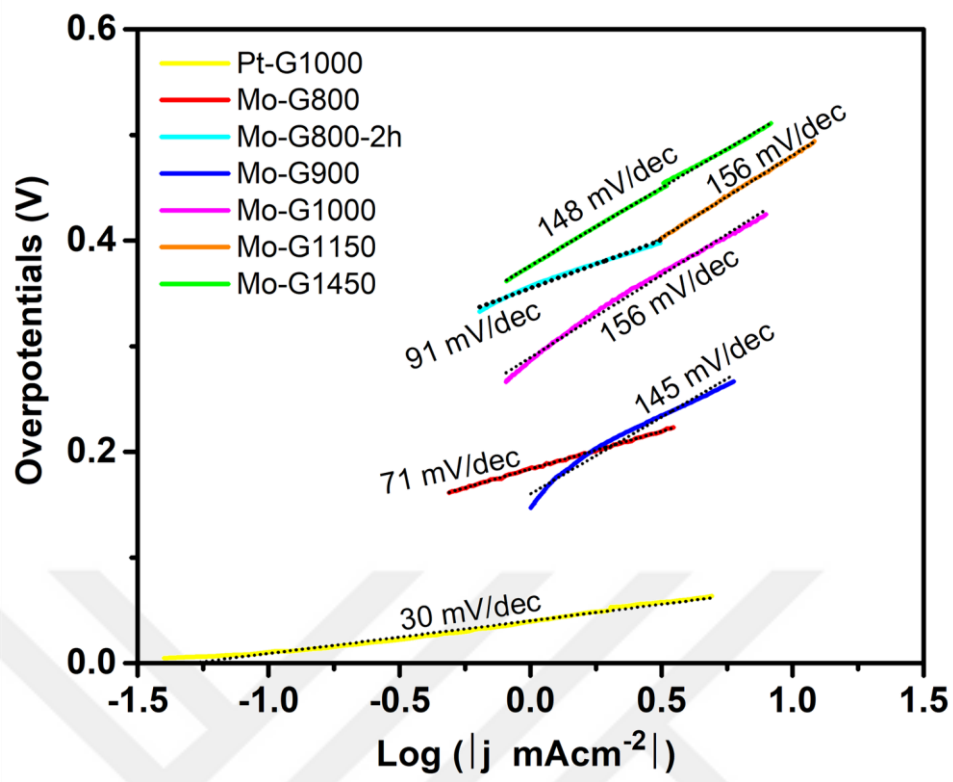


Figure 5.22 Tafel slopes of Mo-based electrodes and Pt-G1000 sample

Table 5.1 shows the onset potentials, overpotentials and Tafel slopes of prepared electrodes. Mo-G800 sample has the lowest overpotential and Tafel slope amongst Mo-based electrodes.

Table 5.1 Catalytic activity results of prepared electrodes

Electrode	Tafel Slope *mV/dec*	η_0 *mV*	η_{10} *mV*
Bare Graphite	-	492	-
Pt-G500	-	74	110
Pt-G1000	30	39	80
Mo-G800-2h	91	357	466
Mo-G800	71	174	270
Mo-G900	145	147	299
Mo-G1000	156	143	386
Mo-G1150	156	294	480
Mo-G1450	148	376	525

5.16 Stability Tests of Mo-G800 and Mo-G900 Samples

The LSV curve of the Mo-G800 sample recorded before and after 1000 CV cycles is shown in Fig. 5. 23. A shift toward higher overpotentials might originate either from poor anchoring of Mo NPs to the graphite substrate or some reduction reaction associated with the existing molybdenum oxide (thin layer).

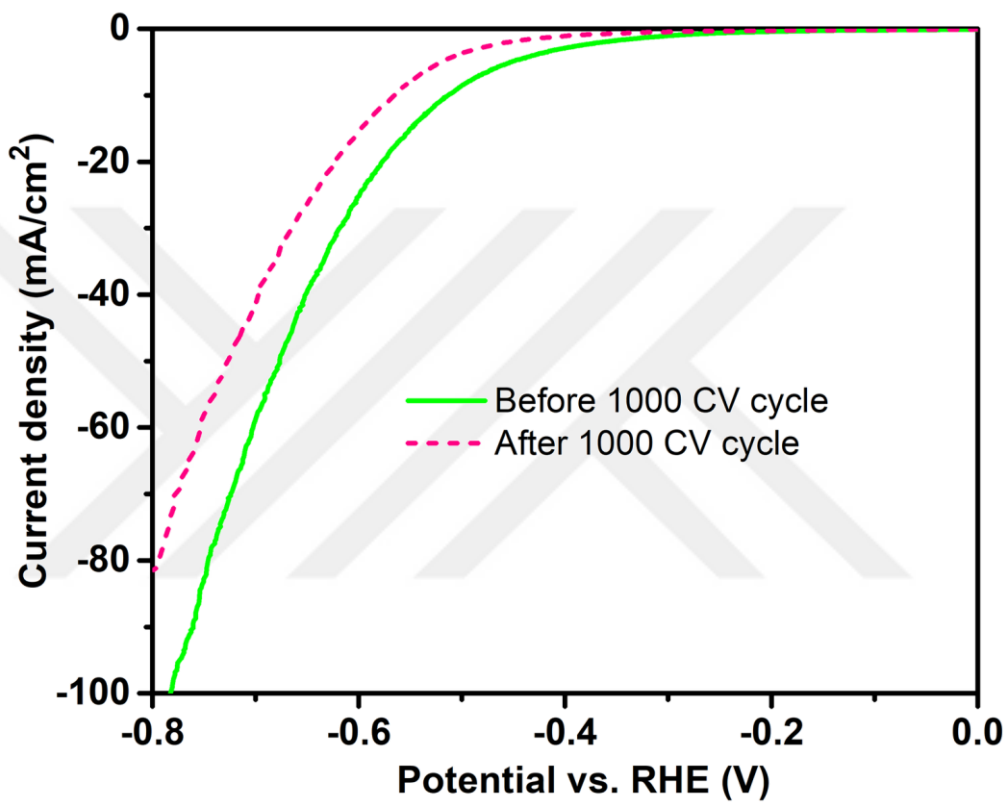


Figure 5.23 LSV curves of Mo-G800 sample in 0.5M H_2SO_4 recorded at 2 mV/s before and after1000 CV cycles

Stability tests were also performed for the Mo-G900 sample. In this case the stability tests show no difference in the LSV curves before and after the cyclic test (1000 cycles) as shown in Fig 5.24. This reveals that, the Mo-G900 sample has excellent stability and durability towards HER. As reported by other researchers, Mo-based materials exhibit good stability against corrosion [52]. The stability of Mo-G800 and Mo-G900 samples can be explained with the recorded SEM images. It looks like the attachment of Mo NPs in Mo-G900 sample is better since they are embedded deeper within graphite layers. Another difference between the two samples is related to

crystallinity. The Mo NPs in the Mo-G900 are crystalline, compared with those are amorphous in the Mo-G800. As a result of crystallinity and better anchoring, the Mo-G900 sample exhibits better stability and durability.

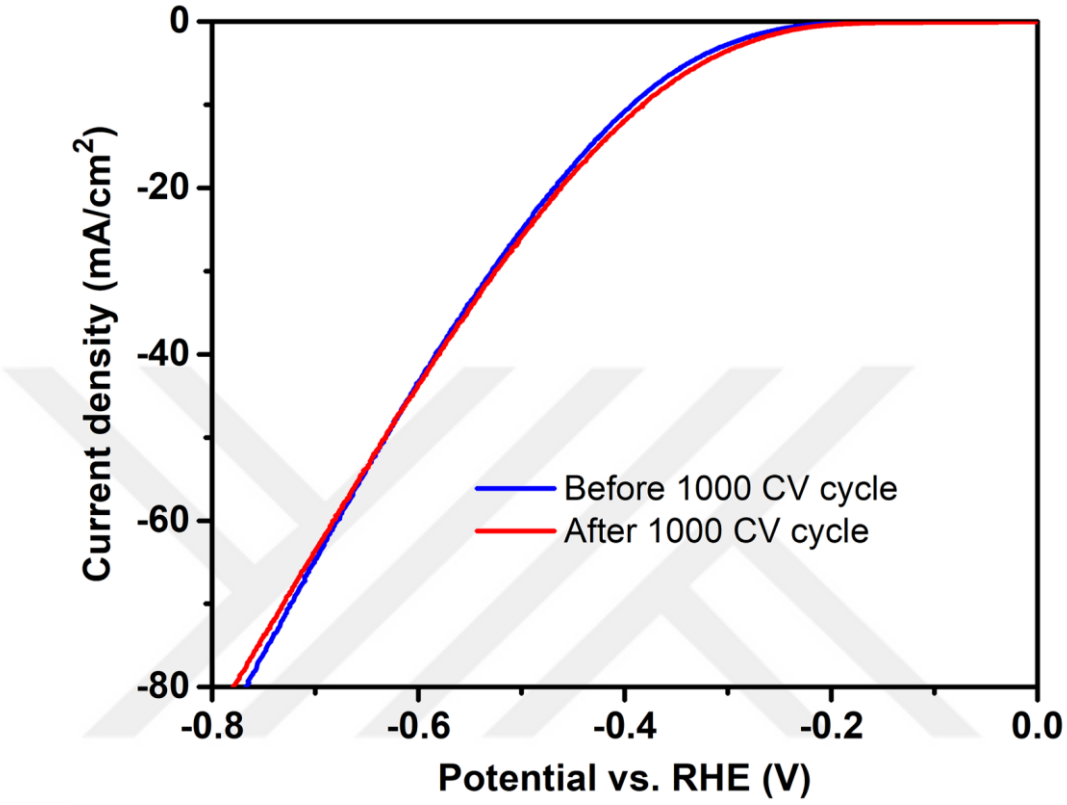


Figure 5.24 LSV curves of Mo-G900 sample in 0.5M H_2SO_4 recorded at 2 mV/s before and after 1000 CV cycles

5.17 Electrochemical Impedance Spectroscopy (EIS) of Mo-G800 Sample

Fig. 5.25 depicts the resistance of the Mo-G800 electrode. The decrease of charge transfer resistance (R_{ct}) with the increasing of applied bias voltage is given in Fig. 5.25 (b). The Mo-G800 exhibits R_{ct} as low as 12 ohms at an applied bias of -300 mV (RHE) which is consistent to its LSV results. The overpotential recorded during the LSV measurements for this sample is 270 mV. As expected, when applied bias is higher than this overpotential, a charge transfer process is facilitated between electrode surface and electrolyte and the R_{ct} approaches zero.

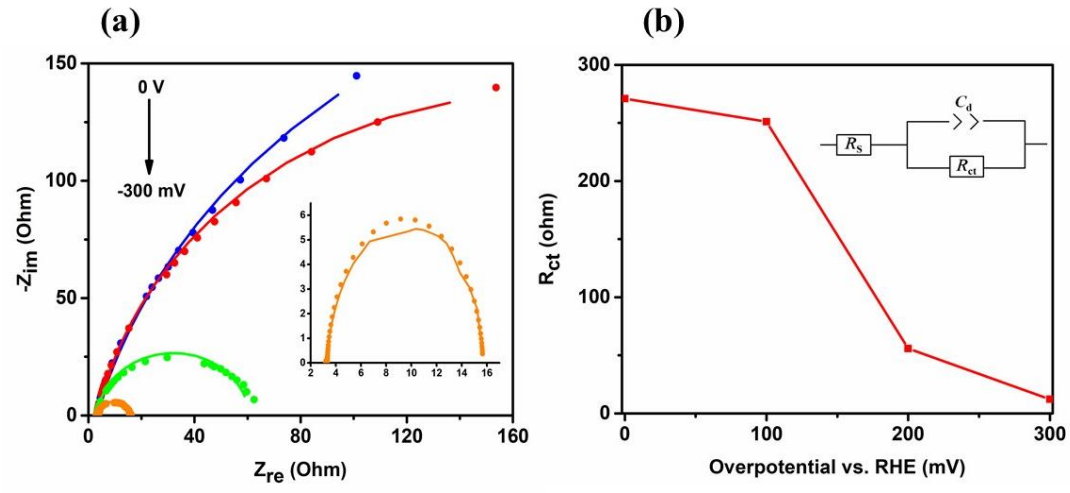


Figure 5.25 (a) Nyquist plot of Mo-G800 sample recorded with a bias voltage from 0 to -300 mV (RHE). In (a) the inset is the Nyquist plot recorded with a bias -300 mV. (b) Charge transfer resistance vs overpotential. The inset in (b) is the equivalent circuit model used for fitting

Table 5.2 shows results for R_{ct} and double layer capacitance (C_d) of the Mo-G800 sample. The recorded EIS data were fitted using an equivalent circuit model as shown in the inset of Fig. 5. 25 (b).

Table 5.2 Electrochemical impedance spectroscopy results of Mo-G800 sample

Bias *(V RHE)*	Series Res. (ohm)	Error (%)	Charge Transfer Res. (ohm)	Double Layer Capacitance $(\times \mathbf{10^{-1}}\ F)$
0	4.79	12	271	6.11
-100	4.12	12.77	251	4.56
-200	3.43	6.83	55.79	3.05
-300	3.34	2.71	12.19	2.79

CHAPTER 6

6 CONCLUSION

The LSV findings reveal that annealing temperature has a strong effect on obtained electrocatalytic activities. The obtained XRD data allowed us to understand the composition of the samples and explain the observed LSV results. It was found that the Mo-G800 sample exhibits the lowest overpotential (-270 mV) and shows the highest electrocatalytic activity towards HER. However, it shows lower stability when compared with the Mo-G900 sample. The reason for the Mo-G800 presenting low overpotential might be that amorphous Mo NPs have small sizes (~4 nm) and relatively good anchoring to the substrate. On the other hand, the samples containing Mo_2C phase prepared using the protocol developed in this thesis show higher overpotential values. Therefore, the samples containing the Mo_2C phase are less attractive for HER applications than their metallic thin film counterparts. We used a combination of methods such as TEM, SEM, EDX, CV, LSV and EIS to gain deeper understanding of composition, morphology and catalytic activities of the presented Mo and Mo_2C thin films.

REFERENCES

[1] A. Veziroglu, R. Macario, Fuel cell vehicles: State of the art with economic and environmental concerns, International Journal of Hydrogen Energy, 36 (2011) 25-43.

[2] G. Nicoletti, N. Arcuri, G. Nicoletti, R. Bruno, A technical and environmental comparison between hydrogen and some fossil fuels, Energy Conversion and Management, 89 (2015) 205-213.

[3] T. da Silva Veras, T.S. Mozer, D. da Costa Rubim Messeder dos Santos, A. da Silva César, Hydrogen: Trends, production and characterization of the main process worldwide, International Journal of Hydrogen Energy, 42 (2017) 2018-2033.

[4] I. Dincer, Renewable energy and sustainable development: a crucial review Renewable and Sustainable Energy Reviews, 4 (2000) 157-175.

[5] A. Yilanci, I. Dincer, H.K. Ozturk, A review on solar-hydrogen/fuel cell hybrid energy systems for stationary applications, Progress in Energy and Combustion Science, 35 (2009) 231-244.

[6] C. Acar, I. Dincer, Comparative assessment of hydrogen production methods from renewable and non-renewable sources, International Journal of Hydrogen Energy, 39 (2014) 1-12.

[7] C. Acar, I. Dincer, Impact assessment and efficiency evaluation of hydrogen production methods, International Journal of Energy Research, 39 (2015) 1757-1768.

[8] I. Dincer, C. Acar, Review and Evaluation of Hydrogen Production Methods for Better Sustainability, Alternative Energy and Ecology (ISJAEE), (2016) 14-36.

[9] A. Midilli, M. Ay, I. Dincer, M.A. Rosen, On hydrogen and hydrogen energy strategies, Renewable and Sustainable Energy Reviews, 9 (2005) 255-271.

[10] M.I. Jamesh, Recent progress on earth abundant hydrogen evolution reaction and oxygen evolution reaction bifunctional electrocatalyst for overall water splitting in alkaline media, Journal of Power Sources, 333 (2016) 213-236.

[11] M. Zeng, Y. Li, Recent advances in heterogeneous electrocatalysts for the hydrogen evolution reaction, Journal of Materials Chemistry A, 3 (2015) 14942-14962.

[12] T.L. LeValley, A.R. Richard, M. Fan, The progress in water gas shift and steam reforming hydrogen production technologies – A review, International Journal of Hydrogen Energy, 39 (2014) 16983-17000.

[13] M. Tahir, L. Pan, F. Idrees, X. Zhang, L. Wang, J.-J. Zou, Z.L. Wang, Electrocatalytic oxygen evolution reaction for energy conversion and storage: A comprehensive review, Nano Energy, 37 (2017) 136-157.

[14] D.D. Vasić Anićijević, V.M. Nikolić, M.P. Marčeta-Kaninski, I.A. Pašti, Is platinum necessary for efficient hydrogen evolution? – DFT study of metal monolayers on tungsten carbide, International Journal of Hydrogen Energy, 38 (2013) 16071-16079.

[15] N.S. Alhajri, D.H. Anjum, K. Takanabe, Molybdenum carbide–carbon nanocomposites synthesized from a reactive template for electrochemical hydrogen evolution, J. Mater. Chem. A, 2 (2014) 10548-10556.

[16] Y. Zhong, X. Xia, F. Shi, J. Zhan, J. Tu, H.J. Fan, Transition Metal Carbides and Nitrides in Energy Storage and Conversion, Adv Sci (Weinh), 3 (2016) 1500286.

[17] Z. Shi, K. Nie, Z.-J. Shao, B. Gao, H. Lin, H. Zhang, B. Liu, Y. Wang, Y. Zhang, X. Sun, X.-M. Cao, P. Hu, Q. Gao, Y. Tang, Phosphorus-Mo_2C@carbon nanowires toward efficient electrochemical hydrogen

evolution: composition, structural and electronic regulation, Energy & Environmental Science, 10 (2017) 1262-1271.

[18] R. Ma, Y. Zhou, Y. Chen, P. Li, Q. Liu, J. Wang, Ultrafine Molybdenum Carbide Nanoparticles Composited with Carbon as a Highly Active Hydrogen-Evolution Electrocatalyst, Angew Chem Int Ed Engl, 54 (2015) 14723-14727.

[19] M. Fan, H. Chen, Y. Wu, L.-L. Feng, Y. Liu, G.-D. Li, X. Zou, Growth of molybdenum carbide micro-islands on carbon cloth toward binder-free cathodes for efficient hydrogen evolution reaction, Journal of Materials Chemistry A, 3 (2015) 16320-16326.

[20] M. Miao, J. Pan, T. He, Y. Yan, B.Y. Xia, X. Wang, Molybdenum Carbide-Based Electrocatalysts for Hydrogen Evolution Reaction, Chemistry, 23 (2017) 10947-10961.

[21] Kopoen, J. Review of water electrolysis technologies and design of renewable hydrogen production systems. Unpublished master dissertation, Lappeenranta University of Technology. 2015.

[22] Iwu, O. M. Solid-state photoelectrochemical hydrogen generation, Doctoral dissertation, University of Oslo. 2013.

[23] M. Carmo, D.L. Fritz, J. Mergel, D. Stolten, A comprehensive review on PEM water electrolysis, International Journal of Hydrogen Energy, 38 (2013) 4901-4934.

[24] Jacobs, J. Economic modeling of cost effective hydrogen production from water electrolysis by utilizing Iceland's Regulating Power Market, Master Dissertation, Reykjavik University. 2016.

[25] Papagiannakis, I. Studying and İmproving the efficiency of water electrolysis using a proton exchange membrane electrolyser, Unpublished master dissertation, Strathclyde University. 2005.

[26] I. Roger, M.A. Shipman, M.D. Symes, Earth-abundant catalysts for electrochemical and photoelectrochemical water splitting, Nature Reviews Chemistry, 1 (2017) 0003.

[27] Merrill, M. D. Water electrolysis at the thermodynamic limit, Unpublished doctoral dissertation, Florida State University. 2007.

[28] Lasia, A. Hydrogen evolution reaction, Handbook of Fuel Cells – Fundamentals, Technology and Applications.(2nd Edition) pp(417). Chichester: John Wiley & Sons Ltd, 2003, (2010).

[29] Oruc, M. E. Energy analysis and fabrication of photovoltaic thermal water electrolyzer and ion transport through modified nanoporous membranes, Unpublished doctoral dissertation, University of Illinois. 2014.

[30] Zlotorowicz, A. Electrocatalysts for medium temperature PEM water electrolysis, Unpublished doctoral dissertation, Norwegian University of Science and Technology. 2013.

[31] Zeng, K. Improvements and Optimisation of Water Electrolysis for Hydrogen Production, Unpublished doctoral dissertation, The University of Western Australia. 2012.

[32] Rasten, E. Electrocatalysis in Water Electrolysis with Solid Polymer Electrolyte, Unpublished doctoral dissertation, Norwegian University of Science and Technology. 2001.

[33] Savant, S. A. Accelerated stress testing protocols of proton exchange membrane (PEM) electrolyzers, Unpublished master dissertation, Karlsruhe Institute of Technology. 2017.

[34] J. Heveling, Heterogeneous Catalytic Chemistry by Example of Industrial Applications, Journal of Chemical Education, 89 (2012) 1530-1536.

[35] Brownson, D. A. C, Banks, C. E. "The Handbook of Graphene Electrochemistry, DOI: 10.1007/978-1-4471-6428-9_2, Springer-Verlag London Ltd. 2014, (2014) 23-77, 23-77.

[35] Bard, A. J., Faulkner,L. R. "Electrochemical Methods" New York: John Wiley & Sons, INC., ISBN 0-471-04372-9.

[37] Hansen, M.K. PEM Water Electrolysis at Elevated Temperatures, Unpublished doctoral dissertation, Technical University of Denmark. 2012.

[38] Pohl, M.D. Identification of active sites at model platinum electrocatalysts, Unpublİshed doctoral dİssertaİton, Technical University of Munich. 2017.

[39] B. Łosiewicz, M. Popczyk, I. Napłoszek, A. Budniok, Intermetallic Compounds as Catalysts in the Reaction of Electroevolution/Absorption of Hydrogen, Solid State Phenomena, 228 (2015) 16-22.

[40] Zoulias, E., Varkaraki, E., Lymberopoulos, N., Christodoulou, C. N., Karagiorgis, G. N. A review on water electrolysis. Retrieved June, 01, 2018 from http://hydrogenoman.com/docs/click%20on%20the%20attached.pdf

[41] Neagu C., Jansen H., Gardeniers H., Elwenspoek M. The electrolysis of water: An actuation principle for MEMS with a big opportunity. Mechatronics, (10), 571-581. 2000.

[42] Bernsmeir, D.B. Noble metal nanoparticles supported in ordered mesoporous carbon coatings as efficient electrocatalysts for the hydrogen evolution reaction, Unpublİshed doctoral dissertation, Technical University of Berlin. 2017.

[43] Colombo, A. Preparation and performance evaluation of materials for electrocatalytic applications, Unpublished doctoral thesis, Università Degli Studi Di Milano. 2010.

[44] S. Emin, C. Altinkaya, A. Semerci, H. Okuyucu, A. Yildiz, P. Stefanov, Tungsten carbide electrocatalysts prepared from metallic tungsten

nanoparticles for efficient hydrogen evolution, Applied Catalysis B: Environmental, 236 (2018) 147-153.

[45] What is Spin Coating. (n.d). Retrieved June 1, 2018, from http://www.spincoater.com/what-is-spin-coating.php.

[46]. O. Olea-Mejia, R. Contreas-Bulnes, C.M. Zamudio-Ortega, R. A. Morales-Luckie, O. Olea-Cardoso, R. López-Castañares. "Scanning Electron Microscopy and Energy Dispersive Spectroscopy microanalysis applied to human dental specimens under laser irradiation for caries prevention", Microscopy: Advances in Scientific Research and Education, (2014).Retrieved June 01, 2018, from http://www.formatex.info/microscopy6/book/70-77.pdf.

[47] S. Emin, M. Fanetti, F.F. Abdi, D. Lisjak, M. Valant, R. van de Krol, B. Dam, Photoelectrochemical properties of cadmium chalcogenide-sensitized textured porous zinc oxide plate electrodes, ACS Appl Mater Interfaces, 5 (2013) 1113-1121.

[48] J. Guardia-Valenzuela, A. Bertarelli, F. Carra, N. Mariani, S. Bizzaro, R. Arenal, Development and properties of high thermal conductivity molybdenum carbide - graphite composites, Carbon, 135 (2018) 72-84.

[49] Morris, M. C., McMurdie, H. F., Evans, E. H., Paretzkin, B., Parker, H. S., Wong-Ng, W., Gladhill, D. M.,Hubbard C. R. "Standards X-ray diffraction powder patterns. Section 17: Data for 54 substances" Washington, DC: National Bureau of Standards, ~National Measurement Laboratory, U.S. Government Printing Office. September, 1985.

[50] C. Ge, P. Jiang, W. Cui, Z. Pu, Z. Xing, A.M. Asiri, A.Y. Obaid, X. Sun, J. Tian, Shape-controllable synthesis of Mo_2C nanostructures as hydrogen evolution reaction electrocatalysts with high activity, Electrochimica Acta, 134 (2014) 182-186.

[51] S. Jing, L. Zhang, L. Luo, J. Lu, S. Yin, P.K. Shen, P. Tsiakaras, N-Doped Porous Molybdenum Carbide Nanobelts as Efficient Catalysts for Hydrogen Evolution Reaction, Applied Catalysis B: Environmental, 224 (2018) 533-540.

[52] J. Wang, W. Wang, L. Ji, S. Czioska, L. Guo, Z. Chen, Highly Dispersed Mo_2C Nanoparticles Embedded in Ordered Mesoporous Carbon for Efficient Hydrogen Evolution, ACS Applied Energy Materials, 1 (2018) 736-743.

CURRICULUM VITAE

PERSONAL INFORMATION



Name Surname : Cesur ALTINKAYA
Date of Birth : 21.08.1990
E-mail : cesuraltnky@gmail.com

EDUCATION

High School : Rize Science High School
Bachelor : Blacksea Technical University (3.16/4)
Master Degree : Ankara Yıldırım Beyazıt University (continued)

WORK EXPERIENCE

Research Assist. : Ankara Yıldırım Beyazıt University (2016-continued)
Türk-Alman University (2016 March-October)

TOPICS OF INTEREST

- Renewable Energy
  Hydrogen Production
  Perovskite Solar Cell

PUBLICATIONS (SCI)

(2018)

1. S. Emin, **C. Altinkaya**, A. Semerci, H. Okuyucu, A. Yildiz**,** P. Stefanov "Tungsten carbide electrocatalysts prepared from metallic tungsten nanoparticles for efficient hydrogen evolution" Applied Catalysis B: Environmental 236 (2018) 147

CONFERENCE PROCEEDINGS

(2018)

1. **C. Altinkaya**, S. Emin, A. Yildiz, M. Valant "Molybdenum carbide thin films for electrochemical water splitting reactions'' International Conference on Physical Chemistry and Functional Materials (Elazıg, Turkey), p192 (2017)
2. **C. Altinkaya**, S. Emin, A. Semerci, A. Yildiz, P. Stefanov, M. Valant "Tungsten carbide thin films for hydrogen evolution reactions'' International Conference on Physical Chemistry and Functional Materials (Elazıg, Turkey), (2018)
3. **C. Altinkaya**, S. Emin, A. Yıildiz, M. Valant "Pt/C@W/C composite thin films for hydrogen evolution reactions'' International Conference on Physical Chemistry and Functional Materials (Elazıg, Turkey), (2017)
4. Atli, A. Atilgan, K. Ozel, Z. K. Yildiz, **C. Altinkaya**, A. Yildiz, '' Multilayer dye sensitized solar cell structures'' International Conference on Photovoltaic Science and Technologies (Ankara, Turkey), p130 (2018)
5. Atli, A. Atilgan, K. Ozel, Z. K. Yildiz, **C. Altinkaya**, A. Yildiz, ''Enhancement of light absorption ability of DSSCs with designing of multilayer photoanode'' International Conference on Photovoltaic Science and Technologies (Ankara, Turkey), p131 (2018)
6. Z. K. Yildiz, A. Atilgan, A**.** Atli, K. Ozel, **C. Altinkaya**, A. Yildiz, '' Effect of using black mulberry as photosensitizer and TiO_2 having different thickness on the performance of dye-sensitized solar cells'' International Conference on Photovoltaic Science and Technologies (Ankara, Turkey), p135 (2018)
7. Z. K. Yildiz, A. Atilgan, A**.** Atli, K. Ozel, **C. Altinkaya**, A. Yildiz, '' Obtaining dye-sensitized solar cells using 3 natural dyes as sensitizer'' International Conference on Photovoltaic Science and Technologies (Ankara, Turkey), p136 (2018)
8. Atilgan, K. Ozel, Z. K. Yildiz, **C. Altinkaya**, A**.** Atli, A. Yildiz, ''Natural dyes as photosensitizers for dye-sensitized solar cells'' International

Conference on Photovoltaic Science and Technologies (Ankara, Turkey), p140 (2018)

9. K. Ozel, Z. K. Yildiz, **C. Altinkaya**, A**.** Atli, A. Atilgan, A. Yildiz, ‘’Low-cost production of DSSCs’’ International Conference on Photovoltaic Science and Technologies (Ankara, Turkey), p127 (2018)
10. K. Ozel, Z. K. Yildiz, **C. Altinkaya**, A**.** Atli, A. Atilgan, A. Yildiz, ‘Controlling of morphological properties of the photoanode of DSSCs’’ International Conference on Photovoltaic Science and Technologies (Ankara, Turkey), p128 (2018)

(2017)

11. S. Emin, **C. Altinkaya**, H. Okuyucu, M. Valant, A. Yildiz “Tungsten carbide thin films for electrochemical water splitting studies’’ International Conference on Functional Nanomaterials and Nanodevices (Budapest, Hungary), p128 (2017)